

---

# Variational Inference with Hölder Bounds

---

Junya Chen\*  
Duke University

Danni Lu  
Virginia Tech

Zidi Xiu  
Duke University

Ke Bai  
Duke University

Lawrence Carin  
Duke University

Chenyang Tao\*  
Duke University

## Abstract

The recent introduction of thermodynamic integration techniques has provided a new framework for understanding and improving variational inference (VI). In this work, we present a careful analysis of the thermodynamic variational objective (TVO), bridging the gap between existing variational objectives and shedding new insights to advance the field. In particular, we elucidate how the TVO naturally connects the three key variational schemes, namely the importance-weighted VI, Rényi-VI and MCMC-VI, which subsumes most VI objectives employed in practice. To explain the performance gap between theory and practice, we reveal how the pathological geometry of thermodynamic curves negatively affect TVO. By generalizing the integration path from the geometric mean to the weighted Hölder mean, we extend the theory of TVO and identify new opportunities for improving VI. This motivates our new VI objectives, named the *Hölder bounds*, which flatten the thermodynamic curves and promise to achieve one-step approximation of the exact marginal log-likelihood. A comprehensive discussion on the choices of numerical estimators is provided. We present strong empirical evidence on both synthetic and real-world datasets to support our claims.

## 1 Introduction

One of the key challenges in modern machine learning is to approximate complex distributions. Due to recent advances on learning scalability (Hoffman et al., 2013) and flexibility (Kingma et al., 2016), and the development of automated inference procedures (Ranganath

et al., 2014), *variational inference* (VI) has become a popular approach for general latent variable models (Blei et al., 2017). Variational inference leverages a posterior approximation to derive a lower bound on the log-evidence of the observed data, and it can be efficiently optimized. This variational bound, more commonly known as the *evidence lower bound* (ELBO), serves as a surrogate objective for *maximum likelihood estimation* (MLE). Successful applications of VI have been reported in document analysis (Blei et al., 2003), neuroscience (Friston et al., 2007), generative modeling (Kingma and Welling, 2014), among many others.

A widely recognized heuristic is that, tightening the variational bound, in general, improves model performance (Burda et al., 2016). Consequently, considerable research has been directed toward this goal. The most direct approach seeks to boost the expressive power of the approximate posterior, such that it can match the true posterior better. For instance, normalizing flows (Rezende and Mohamed, 2015; Kingma et al., 2016) exploited invertible transformations with tractable Jacobian on the latent codes, Salimans et al. (2015); Gregor et al. (2015); Ranganath et al. (2016) explored the hierarchical structure of the latent code generation, Miller et al. (2016) modeled the posterior as a mixture of Gaussians, and Mescheder et al. (2017) adversarially trained a neural sampler to enable flexibility. Alternatively, employing data-adaptive priors similarly closes the variational gap (Tomczak and Welling, 2018). While showing varying degree of successes, these approaches often involve specific design choices (*e.g.*, network architectures), which complicates implementations.

Independent of design choices of posteriors and priors, an orthogonal direction instead advocates direct modifications to the variational objectives, making them provably tighter or otherwise more favorable (*e.g.*, efficiency, stability, *etc.*). As a prominent example, the ELBO can be sharpened by leveraging multiple posterior samples weighted in accordance with their importance (Burda et al., 2016). Further, Rényi-VI (Li and Turner, 2016) and  $\chi$ -VI (Dieng et al., 2017) derived a family of variational targets that interpolates between lower and upper bounds to the log-likelihood

---

Preprint. Under review. Correspond to: Junya Chen: junya.chen@duke.edu, Chenyang Tao: chenyang.tao@duke.edu

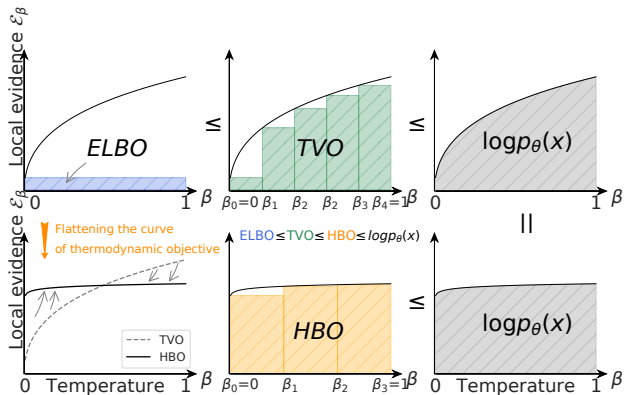


Figure 1: Thermodynamic integration and variational bounds. Marginal likelihood  $\log p_\theta(x)$  equals the area under the thermodynamic curve. We show by carefully choosing an integral path to flatten the thermodynamic curve, the  $\log p_\theta(x)$  can be approximated more accurately and with less computations.

(Tao et al., 2018), and they belong to the more general family of  $f$ -divergence VI (Wan et al., 2020). Bamler et al. (2017) developed a more general view on and presented a low-variance estimator based on a perturbative argument. However, an important note made by Rainforth et al. (2017) is that sharpening the variational bound may inadvertently hurt model inference (*i.e.*, the approximate posterior).

More recently, Masrani et al. (2019) derived a novel variational objective using *Thermodynamic Integration* techniques (Lartillot and Philippe, 2006). This new scheme, known as the *thermodynamic variational objective* (TVO), is defined by a path integral of local evidence curve, which in theory recovers the exact model marginal log-likelihood (see Figure 1 and Sec 2.1). The discrete Riemann left sum of the curve yields lower bounds the log marginal likelihood and is provably sharper than the ELBO. TVO applies widely to continuous, discrete and non-reparametrizable distributions, with competitive performance reported. Perhaps surprisingly, TVO manages to break the tension between the bound tightness and estimator variance (Tao et al., 2018), at the cost of sampling transition distributions along the integral path.

While TVO points to new directions for advancing variational inference, there are important open questions to be answered: (a) How is this TVO connected to the existing vast literature on VI? (b) Is the convenient choice of geometric path optimal? If not, what is a feasible, more favorable alternative? (c) Implementation-wise, what are the trade-offs between different numerical strategies? (d) Why TVO failed to deliver the promised exact inference even on toy problem?

In this study, we seek answers to the above ques-

tions, in the hope that our insights and observations can serve to better understand and guide the practice of TVO as well as other advanced VI schemes. In particular, our key contributions include: (i) Clarification of how TVO recovers major VI schemes, including importance-weighted (IW) VAE, Rényi-VI and MCMC-VI; (ii) careful analysis of TVO wrt the more general Hölder path integrals, extending theoretical results and motivating novel VI objectives named HBO; (iii) practical discussions on the choice of numerical schemes for thermodynamic variational schemes, covering important topics such as trade-offs and automated parameter tuning.

## 2 Thermodynamic Objectives for Variational Inference

We first review the basics of TVO and its role in inference, and then elaborate on the important connections to other well-established VI schemes (*e.g.*, IW-VAE, Rényi-VI and MCMC-VI).

### 2.1 Thermodynamic integration and VI

**Thermodynamic integration.** Assume we have two unnormalized distributions  $\tilde{\pi}_0(z)$  and  $\tilde{\pi}_1(z)$ , with  $Z_0$  and  $Z_1$  as their respective normalizing constants (*i.e.*,  $\int \tilde{\pi}_i(z) dz / Z_i = 1, i \in \{0, 1\}$ ). Thermodynamic integration allows us to compute the log ratio  $\log \frac{Z_1}{Z_0}$  between the normalization constants via integrating over a path  $\tilde{\pi}_\beta$  that interpolates between  $\tilde{\pi}_0$  and  $\tilde{\pi}_1$ . Let  $\pi_\beta = \tilde{\pi}_\beta / Z_\beta$  be the normalized form of some intermediate unnormalized density  $\tilde{\pi}_\beta$  for  $\beta \in [0, 1]$ , with  $Z_\beta = \int \tilde{\pi}_\beta(z) dz$  as its normalizing constant. We further denote its potential function as  $U_\beta(z) \triangleq \log \tilde{\pi}_\beta(z)$ . Then the following identity immediately follows from (Masrani et al., 2019)

$$\begin{aligned} \log Z_1 - \log Z_0 &= \int_0^1 \partial_\beta \{\log Z_\beta\} d\beta \\ &= \int_0^1 \mathbb{E}_{Z \sim \pi_\beta} [\partial_\beta U_\beta(Z)] d\beta. \end{aligned} \quad (1)$$

**Variational inference.** For a latent variable model  $p_\theta(x, z)$ , we consider  $x$  as an observation (*i.e.*, data) and  $z$  as the latent variable we want to infer. The marginal likelihood  $p_\theta(x) = \int p_\theta(x, z) dz$  typically does not have a closed-form expression, and to avoid direct numerical estimation of  $p_\theta(x)$ , VI instead optimizes a variational bound to the marginal log-likelihood. The most popular choice is known as the *Evidence Lower Bound* (ELBO), given by

$$\text{ELBO} \triangleq \mathbb{E}_{Z \sim q_\phi(z|x)} \left[ \log \frac{p_\theta(x, Z)}{q_\phi(Z|x)} \right] \leq \log p_\theta(x), \quad (2)$$

where  $q_\phi(z|x)$  is an approximation to the true posterior  $p_\theta(z|x)$  and the inequality is a direct result of Jensen's inequality. This bound tightens as  $q_\phi(z|x)$  approaches

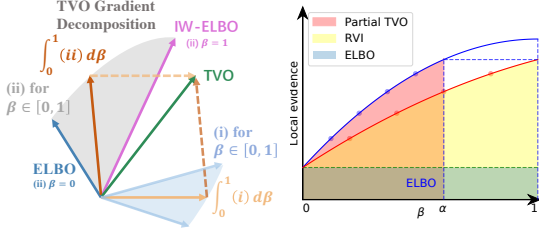


Figure 2: (Left) TVO gradient can be factorized into an interpolation between the ELBO and IW-ELBO gradients (Eq.(9) term (ii)) plus a REINFORCE gradient correction (Eq.(9) term (i)). (Right) The  $\alpha$ -Rényi variational bound (yellow) is equivalent to partially integrated TVO bound (red) rescaled with  $\frac{1}{\alpha}$ .

the true posterior  $p_\theta(z|x)$ . For estimation, we seek parameters  $\theta$  that maximize the ELBO, and the commensurately learned parameters  $\phi$  are often used in a subsequent inference task with new data.

**Thermodynamic variational objective.** To connect VI to TVO, let us set  $\tilde{\pi}_0 = q_\phi(z|x)$ ,  $\tilde{\pi}_1 = p_\theta(x, z)$ , and conveniently choose the *geometric mean* path

$$\tilde{\pi}_\beta(z) = \tilde{\pi}_1^\beta \tilde{\pi}_0^{1-\beta} = p_\theta(x, z)^\beta q_\phi(z|x)^{1-\beta} \quad (3)$$

between the posterior approximation  $q_\phi$  and model distribution  $p_\theta$ . Simple computation reveals

$$\log Z_1 = \log p_\theta(x), \log Z_0 = 0, \partial_\beta U_\beta(z) = \log \frac{p_\theta(x, z)}{q_\phi(z|x)}. \quad (4)$$

Plugging these into (1), it gives us

$$\log p_\theta(x) = \int_0^1 \mathcal{E}_\beta d\beta, \quad \mathcal{E}_\beta \triangleq \mathbb{E}_{Z_\beta \sim \pi_\beta} \left[ \log \frac{p_\theta(x, Z_\beta)}{q_\phi(Z_\beta|x)} \right]. \quad (5)$$

To simplify our discussion, hereafter we refer to  $\mathcal{E}_\beta$  as the *local evidence*, which recovers the classical ELBO when  $\beta = 0$  and becomes an upper bound to the likelihood at  $\beta = 1$  (denoted as EUBO). That is to say, when following a geometric mean path, the log evidence  $\log p_\theta(x)$  can be expressed as the integration of local evidence along the path. To construct practical estimators from (5), one can partition the unit interval  $[0, 1]$  into  $K$  discrete bins  $\{\beta_k\}_{k=0}^K$  and integrate the local evidence with left Riemann sum as

$$\text{TVO} = \sum_k (\beta_{k+1} - \beta_k) \mathcal{E}_{\beta_k}. \quad (6)$$

The main result from the original TVO paper (Masrani et al., 2019) is that  $\mathcal{E}_\beta$  is a non-decreasing function of  $\beta$ , *i.e.*,  $\mathcal{E}_\beta \leq \mathcal{E}_{\beta'}$  for  $\beta < \beta'$ , which implies

$$\text{ELBO} \leq \text{TVO} \leq \log p_\theta(x), \quad (7)$$

And the gap  $\mathbb{D}(q(z|x) \parallel p(z|x)) \triangleq \log p(x) - \text{TVO}$  defines a specific divergence measure between  $q(z|x)$  and  $p(z|x)$  (Brekelmans et al., 2020), *i.e.*,  $\mathbb{D}(q(z|x) \parallel p(z|x)) \geq 0$  with the equality holds iff  $p(z|x) = q(z|x)$ .

## 2.2 Bridging the gap

A missing piece in the original work of Masrani et al. (2019) is the TVO’s connection to the more recent developments in the VI literature. We contribute this section to the discussion of the inherent connections between TVO and other prominent examples of advanced VI schemes, which all seek to improve the bound. Technical derivations are deferred to the *supplementary material* (SM) Sec. C.

**Importance-weighted VAE (Burda et al., 2016)** uses multiple latent samples to tighten the variational bound. In particular, the importance-weighted ELBO is given by

$$\text{IW-ELBO} = \mathbb{E}_{Z_{1:S} \sim q_\phi} \left[ \log \left\{ \frac{1}{S} \sum_s \frac{p_\theta(x, Z_s)}{q_\phi(Z_s|x)} \right\} \right], \quad (8)$$

where  $\{Z_s\}$  are  $S$  independent samples from  $q_\phi$  and IW-ELBO is provably tighter than the vanilla ELBO. The empirical estimator for TVO also employed self-normalized importance weights, using  $q_\phi$  as the proposal distribution. The importance weights for  $\pi_\beta$  are then given by  $w_s^\beta = \tilde{w}_s^\beta / (\sum_s \tilde{w}_s^\beta)$ , where  $\tilde{w}_s = p_\theta(x, Z_s) / q_\phi(Z_s)$  denotes the unnormalized importance weights and  $Z_s \sim q_\phi(z|x)$ . TVO uses the following estimator to compute the gradients of  $\lambda \triangleq (\theta, \phi)$

$$\begin{aligned} \nabla_\lambda \mathcal{E}_\beta &= \mathbb{E}_{\pi_\beta} [\nabla_\lambda f_\lambda] + \text{cov}_{\pi_\beta} [\nabla_\lambda \log \tilde{\pi}_\beta(\lambda), f_\lambda] \\ \nabla_\lambda \hat{\mathcal{E}}_\beta &= \sum_s \underbrace{w_s^\beta \nabla_\lambda \log \tilde{\pi}_\beta(Z_s) (f_\lambda(Z_s) - \bar{f}_\lambda)}_{(i)} + \sum_s \underbrace{w_s^\beta \nabla_\lambda f_\lambda(Z_s)}_{(ii)}, \end{aligned} \quad (9)$$

where  $f_\lambda(z) \triangleq \log \frac{p_\theta(x, z)}{q_\phi(z|x)}$ ,  $\bar{f}_\lambda \triangleq \sum_s w_s^\beta f_\lambda(Z_s)$ . Note the (i) term is the REINFORCE gradient of the ELBO (Williams, 1992)<sup>1</sup>. When  $\beta \in \{0, 1\}$ , the (ii) term coincides with the ELBO’s and IW-ELBO’s gradient respectively. This helps enforce the view that TVO is a generalization of standard bounds with annealed importance weights, enhanced with additional REINFORCE gradient corrections (see Figure 2).

**Rényi variational inference (Li and Turner, 2016; Dieng et al., 2017; Tao et al., 2018)** While vanilla VI minimizes the KL-divergence between the approximate and true posterior, Rényi-VI instead (implicitly) optimizes the more general Rényi-divergence (Rényi et al., 1961), also known as the  $\alpha$ -divergence or  $\chi$ -divergence. Specifically, Rényi-VI targets the following objective

$$\text{RVI}_\alpha \triangleq \frac{1}{\alpha} \log \mathbb{E}_{Z \sim q_\phi} \left[ \left( \frac{p_\theta(x, Z)}{q_\phi(Z|x)} \right)^\alpha \right], \quad (10)$$

where  $\alpha > 0$  and  $\text{RVI}_0 \triangleq \lim_{\alpha \rightarrow 0} \text{RVI}_\alpha$ . Note that  $\text{RVI}_\alpha$  is a non-decreasing function of  $\alpha$ , and the fol-

<sup>1</sup>We note that while the original TVO paper claim to be “REINFORCE-free”, the derived gradient estimator is actually an instantiation of the REINFORCE gradient.

lowing relation holds

$$\begin{aligned} \text{RVI}_0 &= \text{ELBO}, & \text{RVI}_1 &= \log p_\theta(x), \\ \text{ELBO} &\leq \text{RVI}_{\alpha \in (0,1)} \leq \log p_\theta(x) \leq \text{RVI}_{\alpha > 1}. \end{aligned} \quad (11)$$

In simple words, for  $\alpha \in [0, 1]$ , the bound is tighter for a larger  $\alpha$ . The following result explicitly connects RVI to TVO, showing RVI is essentially a re-scaled version of partially integrated TVO (see Figure 2).

**Proposition 2.1.** If  $\alpha \in [0, 1]$ , then  $\text{RVI}_\alpha = \frac{1}{\alpha} \int_0^\alpha \mathcal{E}_\beta d\beta$ .

To clarify the implications from the above Proposition, we recall two major issues with the direct implementation of RVI (Tao et al., 2018): (i) practical estimators are not guaranteed to be a lower bound; (ii) for large  $\alpha$ , it suffers from the variance-tightness trade-off. These are due to the disconnection between theoretical definition and practical estimation, and the integrand in (10) is very unstable for larger values of  $\alpha$ . Our insight implies RVI can be equivalently implemented with thermodynamic integrations, which is guaranteed to be a lower bound and it partly solves the variance issue as the integrand  $\mathcal{E}_\beta$  is now expressed in the more stable log-scale<sup>2</sup>. Further, the Rényi interpretation lends insight for understanding the mode-covering behavior of the inference distribution  $q_\phi(z|x)$ . As discussed in Li and Turner (2016), the approximate posterior  $q_\phi(z|x)$  transitions from mode-seeking to mode-covering as we gradually increase  $\alpha$ .

**MCMC variational inference (Salimans et al., 2015)** belongs to a more general family of VI schemes known as the *Auxiliary VI (Aux-VI)* (Maaløe et al., 2016), which seeks to improve bound sharpness via introducing additional auxiliary variables  $\tilde{z}$ . Due to space limit, we show details on how MCMC-VI recover TVO in the SM Sec. A.

### 3 Hölder Bound Objective: A Hölder Path Analysis of Generalized TVO

While the TVO framework puts no restriction on the path  $\{\tilde{\pi}_\beta\}$ , the convenient choice of a geometric mean path yields an elegant solution. A natural question is, can we improve the results by taking an alternative path? This seems an illegitimate question at first glance, since the TVO is already a sharp bound to the log-evidence. We argue that, as the original TVO paper observed, in practice TVO performs characteristically different from its theoretical predictions, and fails to outperform state-of-the-art VI counterparts. In this section, we provide a careful analysis of its failure, and generalize TVO beyond its original scope to seek remedies, inspiring a new family of thermodynamic variational bounds to close this gap.

<sup>2</sup>This is because the use of importance re-weighting removes another major source of variance.

#### 3.1 Limitations of TVO and a heuristic fix

We identify the main culprit for the degenerated performance of TVO as the pathological curvature of the thermodynamic curve  $\mathcal{E}_\beta$ , which apparently offsets in practical terms the theoretical advantage enjoyed by TVO. By taking an alternative integration path, one hopes to improve TVO via attenuating the harmful geometry: a flatter TVO curve allows a sharper approximation to the marginal log evidence given the same or smaller partition budget  $K$  (Figure 2).

To motivate, we first look at the simplest case, with the geometric mean path replaced by the *arithmetic mean* path<sup>3</sup>. We will refer to the corresponding bound as Wasserstein bound (WBO), and with a bit of computation, we have the following assertion.

**Proposition 3.1.** The thermodynamic curve  $\mathcal{E}_\beta^W$  for arithmetic mean path is non-increasing wrt  $\beta$ . Denoting the lower ( $\mathcal{E}_1^W$ ) and upper bound ( $\mathcal{E}_0^W$ ) respectively as WLBO and WUBO, the following inequalities hold

$$\begin{aligned} \frac{1}{p_\theta(x)} \text{ELBO}(x) &\leq \text{WLBO}(x) \leq \log p_\theta(x), \\ \log p_\theta(x) &\leq \text{WUBO}(x) \leq \text{EUBO}(x). \end{aligned} \quad (12)$$

Unfortunately, the above bounds are not very useful for practical considerations. This is because for real-world applications, it is often expected that  $p(x) \ll 1$ , that is to say  $\text{ELBO} < 0$ . As such, the Wasserstein lower bound WLBO is much worse than the ELBO, aggregating the pathological geometry that we intend to fix (see SM Sec. C for more analysis). However, there is a silver lining in the statement: an interesting observation is that, perhaps surprisingly, the monotonicity of the TVO curve has been flipped wrt the Wasserstein geodesic (see Figure 3). This suggests that, by looking for a continuous path  $\mathcal{E}_{\alpha,\beta}$  parameterized by  $\alpha$  which interpolates between the geometric ( $\alpha = 0$ ) and arithmetic ( $\alpha = 1$ ) means, we might be able to find a tipping point  $\alpha^*$  where the monotonicity flips. In that case, the TVO curve is flat and we are able to evaluate the exact log-likelihood at any point along the thermodynamic curve.

#### 3.2 Flattening the curve with Hölder bounds

In order to generalize the integration path, we consider the more general Hölder averaging operation.

**Definition 3.2** (Weighted Hölder mean path). For  $a, b \in \mathbb{R}_+$  and  $\beta \in [0, 1]$ , the weighted Hölder mean  $\mathcal{M}_\alpha(a, b; \beta) \triangleq [\beta a^\alpha + (1 - \beta)b^\alpha]^{\frac{1}{\alpha}}$ , and for  $\alpha = 0$  we use  $\mathcal{M}_0 = \lim_{\alpha \rightarrow 0} \mathcal{M}_\alpha$ .

See Figure S6 in the SM for examples of Hölder paths. We can analogously define the thermodynamic curves

<sup>3</sup>This corresponds to follow the Wasserstein geodesics in the space of probability distributions



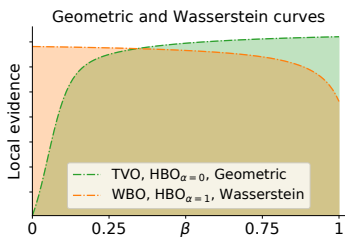


Figure 3: Comparing geometric (green) & Wasserstein (red) thermodynamic curves, the monotonicity is flipped, but area under curve remains the same.

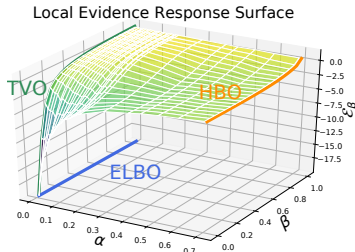


Figure 4: Local evidence surface for the Hölder paths. HBO curve flattens as  $\alpha$  increases, until the monotonicity flips.

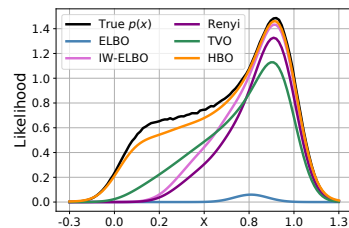


Figure 5: Comparison of approximation accuracy for different variational bounds. Bounds closer to the true  $p(x)$  (black line) is considered better.

wrt Hölder paths, with the following statement directly generalizing the monotonicity result.

**Proposition 3.3.** Under the weighted Hölder mean path  $\tilde{\pi}_{\alpha,\beta} = [\beta\tilde{\pi}_1^\alpha + (1-\beta)\tilde{\pi}_0^\alpha]^{\frac{1}{\alpha}}$ , the Hölder thermodynamic curve given by

$$\mathcal{E}_{\alpha,\beta} = \mathbb{E}_{\tilde{\pi}_{\alpha,\beta}} \left[ \frac{1}{\alpha} \frac{\tilde{\pi}_1^\alpha - \tilde{\pi}_0^\alpha}{\tilde{\pi}_{\alpha,\beta}^\alpha} \right] \quad (13)$$

is non-decreasing with respect to  $\beta$  for  $\alpha \leq 0$  and non-increasing for  $\alpha \geq 1$ .

While Proposition 3.3 does not confirm the existence of such a conjectured tipping point when the curve becomes flat, it predicts where we might be able to find one if it exists. More specifically, such a phase transition point might exist in  $\alpha \in (0, 1)$  for Hölder paths. So motivated, we propose the following new family of Hölder variational objectives that promise to rectify the pathological geometry of TVO.

**Definition 3.4 (Hölder BOunds (HBO)).**

$$\text{HBO}_\alpha \triangleq \int_0^1 \mathcal{E}_{\alpha,\beta} d\beta, \text{ for } \alpha \in (0, 1). \quad (14)$$

**Corollary 3.1.**  $\text{HBO}_\alpha = \log p_\theta(x)$ .

Corollary 3.1 is a direct consequence of the thermodynamic integration equality (1), since the Hölder mean path  $\tilde{\pi}_{\alpha,\beta}$  connects  $\pi_0 = q_\phi(z|x)$  and  $\pi_1 = p_\theta(x, z)$ . With slight abuse of notation, we denote

$$\text{HBO}_\alpha \triangleq \sum_k (\beta_{k+1} - \beta_k) \mathcal{E}_{\alpha,\beta_k} \quad (15)$$

as the empirical HBO estimator, which can be understood as approximations to the log-likelihood.

Figure 4 provides a more intuitive picture via visualizing the Hölder thermodynamic curves wrt different  $\alpha$  (using toy model from our Experiment section). In this example, a non-trivial choice of  $\alpha$  significantly improves the pathological curvature observed in vanilla

TVO, with a wide range of  $\alpha$  yielding relatively flat geometry. In Figure 5, we further show comparisons of different popular variational bounds, presented in the original likelihood scale for better visualization. While our HBO consistently outperforms all its counterparts, TVO underperforms strong baselines (e.g., IW-ELBO, RVI) in many of the regions.

### 3.3 Practical estimation of HBO

**Finding an appropriate  $\alpha$ .** The choice of  $\alpha$  is crucial for the performance of HBO. For a good  $\alpha$ , one can optimally approximate  $\log p_\theta(\mathbf{x})$  with a minimal number of partitions, thus greatly reducing computational overhead. We consider two simple strategies to pick the best  $\alpha$  from a candidate set.

- *Trial & error.* Sample a few test points  $\{\beta_k \in [0, 1]\}$ , evaluate  $\mathcal{E}_{\alpha,\beta}$  at all  $\beta_k$  on candidate  $\alpha$ , choose the one with minimal gap  $\hat{\alpha} = \arg \min_\alpha \{\max_\beta \{\mathcal{E}_{\alpha,\beta}\} - \min_\beta \{\mathcal{E}_{\alpha,\beta}\}\}$ .
- *Binary search.* Assuming the monotonicity of the HBO curve holds, one can use root finding binary search to efficiently locate the optimal  $\alpha$ . Specifically, initialize with  $0 \leq \alpha_L < \alpha_R \leq 1$ , such that  $\mathcal{E}_{\alpha_L,\beta}$  and  $\mathcal{E}_{\alpha_R,\beta}$  are respectively monotonically increasing and decreasing wrt  $\beta$ . Pick  $\alpha_M$  in between  $\alpha_L$  and  $\alpha_R$  (e.g., mid point). If  $\mathcal{E}_{\alpha_M,\beta}$  is increasing wrt  $\beta$ , set  $\alpha_L \leftarrow \alpha_M$ , otherwise  $\alpha_R \leftarrow \alpha_M$ . Repeat this until some stopping criteria is met (e.g.,  $|\alpha_R - \alpha_L|$  or slope of  $\mathcal{E}_{\alpha_M,\beta}$  fall below some tolerance threshold).

The binary search approach is more efficient, but less reliable if the underlying assumption is violated. Note since all  $\mathcal{E}_{\alpha,\beta}$  based on finite-sample empirical estimate using (i.e., a mini-batch of  $z$  sampled from the proposal distribution), one should also properly account for the estimation variance involved.

### Importance-weighted sampling of Hölder path.

To estimate  $\mathcal{E}_{\alpha,\beta}$  one needs to draw samples from the intermediate distributions  $\tilde{\pi}_{\alpha,\beta}$  along the Hölder

path. To avoid the excessive computation entailed by Markov chain Monte-Carlo (MCMC) schemes, we adopt a similar importance weighting strategy employed by the original TVO. In particular, one draws  $B$  samples  $\{z_i\}_{i=1}^B$  from the approximate posterior  $q_\phi(z|x)$ , and then adjusts according to the importance weights  $\tilde{w}_i^\beta \triangleq \tilde{\pi}_{\alpha,\beta}(x, z_i)/q_\phi(z_i)$ . After some algebraic manipulations, the importance weighted local evidence can be expressed as

$$\hat{\mathcal{E}}_{\alpha,\beta}^{\text{IW}} = \frac{1}{\alpha \sum_{i'} (\beta s_{i'} + 1)^{1/\alpha}} \sum_i \frac{s_i}{(\beta s_i + 1)^{1-1/\alpha}}, \quad (16)$$

where  $s_i \triangleq \left(\frac{p_\theta(x, z_i)}{q_\phi(z_i)}\right)^\alpha - 1$ . The corresponding importance-weighted HBO thus writes

$$\widehat{\text{HBO}}_\alpha^{\text{IW}} = \sum_k (\beta_{k+1} - \beta_k) \hat{\mathcal{E}}_{\alpha,\beta_k}^{\text{IW}}. \quad (17)$$

**The perturbed HBO.** While in theory we can directly simulate any Hölder path based on its definition, we might not want to do so for numerical considerations with a larger  $\alpha$ . This is because  $\tilde{\pi}_0$  and  $\tilde{\pi}_1$  typically live on very different scales, and hence a brute-force treatment can potentially lead to catastrophic numerical overflow. Instead, a more interesting regime is where  $\alpha$  is close to zero, in which case both distributions are evaluated near a more comparable log-scale. Inspired by the perturbation argument originally presented in Bamler et al. (2017), we consider a linear expansion near  $\alpha = 0$  wrt the Hölder path. As summarized by the following statement, the perturbed HBO admits a simple expression.

**Proposition 3.5** (Perturbed HBO). For a sufficiently small Hölder parameter  $\delta \ll 1$ , we have the following approximation for integrand  $\partial_\beta U_{\delta,\beta}$  and sampling distribution  $\tilde{\pi}_{\delta,\beta}$

$$\begin{aligned} \partial_\beta U_{\delta,\beta} &\approx \log \frac{p_\theta(x,z)}{q_\phi(z|x)} + \left(\frac{1}{2} - \beta\right) \left[ \log \frac{p_\theta(x,z)}{q_\phi(z|x)} \right]^2 \delta, \\ \log \tilde{\pi}_{\delta,\beta} &\approx [\beta \log \tilde{\pi}_1 + (1 - \beta) \log \tilde{\pi}_0] + \\ &\quad \frac{1}{2} [\beta (\log \tilde{\pi}_1)^2 + (1 - \beta) (\log \tilde{\pi}_0)^2] \delta. \end{aligned} \quad (18)$$

Proposition 3.5 allows us to calibrate vanilla TVO with first-order corrective terms to approximate HBO, which hopefully helps to close the gap between the lower and upper bounds of a TVO curve, thereby “flattening” curvature for improved performance.

## 4 Related Work

**Trade-offs for tightening the variational bounds** have drawn extensive discussions in recent literature. While Rainforth et al. (2017) has argued that tighter bounds may inadvertently hurt inference, we show experimentally that the proposed HBO transcends this trade-off by providing arguments based on both reduced variance and improved effective sample-size, see

our experiments for details. In a similar spirit to Tao et al. (2018), we have leveraged geometric perspectives to improve VI bounds. Closely related is the work of Brekelmans et al. (2020), where the author(s) analyzed the variational gap of TVO in generalized divergence metrics and proposed a smart partition scheme for reduce the estimation gap. Habeck (2017) also discussed issues related to the construction of TVO from physics perspectives. It is possible to further extend the scope to intractable approximate posteriors using adversarial schemes (Mescheder et al., 2017; Dai et al., 2018).

**Energy-based modeling** has close ties to TVO: (i) the marginal likelihood is the partition function of an energy model defined by the joint density; and (ii) TVO-type procedures require sampling from intermediate distributions on the thermodynamic path defined by the energy models. Classical energy-based approaches have focused on estimating the parameters of an unnormalized energy model: MCMC-MLE (Geyer, 1991, 1994), *contrastive divergence* (Hinton, 2002; Du and Mordatch, 2019; Nijkamp et al., 2019), *score matching* (Hyvärinen, 2005), *noise contrastive estimation* (Gutmann and Hyvärinen (2010, 2012); Gutmann and Hirayama (2012)). These schemes often lack a generative perspective and scale less competitively to data complexity. Recently, energy-based perspectives have gain renewed interests in probabilistic learning. Of particular interests are the Stein variational inference (Liu and Wang, 2016; Pu et al., 2017) and Fenchel minimax learning procedures (Dai et al., 2018; Tao et al., 2019a). See also Brekelmans et al. (2020) for a theoretical interpretation of TVO variational gaps using the energy-based exponential family distributions.

**Simulated annealing and thermodynamic integration** have deep connections (Neal, 2001; Frenkel and Smit, 2001), and both have been used to approximate the intractable partition function (Ogata, 1989). Such computational strategies are deeply rooted in non-equilibrium statistical physics (Habeck, 2012; Crooks, 1999; Habeck, 2012, 2017), and have been used for evaluating the data likelihoods for complex models (Wu et al., 2017). While the geometric mean path is dominantly popular, alternative thermodynamic integration paths have also been considered in prior literature: Gelman and Meng (1998) derived a few optimal integration paths for special cases, and Grosse et al. (2013) explored the moment averaged path in the exponential family. Brekelmans et al. (2020) used the moment averaged path to motivate a novel non-uniform partition strategy for TVO that adapts to the shape of the thermodynamic curve. Our HBO instead finds a good thermodynamic path that properly “bends” the curve. A similar perspective was adopted by concurrent work (Masrani et al., 2021) which has different focuses (see SM for clarifications).

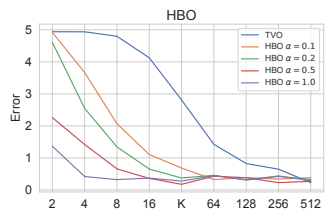


Figure 6: Approximation error for TVO & HBO with different partition size  $K$ .

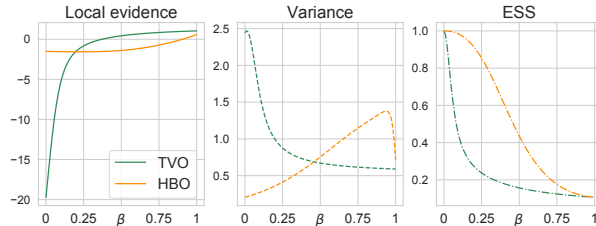


Figure 7: Evidence curve estimation variance and effective-sample size.

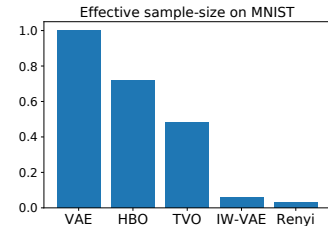


Figure 8: Effective sample-size of different VI objectives on MNIST.

## 5 Experiments

To validate our HBO framework, we consider a wide range of experiments, with synthetic & real-world datasets and state-of-the-art variational schemes. All experiments are implemented with PyTorch<sup>4</sup> and executed on a single NVIDIA TITAN Xp GPU. Details of the experimental setup and extended results are provided in the SM Sec. D. Note our experiments focus on validating theoretical aspects of the HBO framework, the establishment of new state-of-the-art results is beyond the scope of this study.

### 5.1 Synthetic examples: from TVO to HBO

To expose the limitations of existing solutions and demonstrate the appealing features of HBO with a simple example, we synthesize our toy data from  $x \sim \mathcal{N}(\sin(z), 10^{-2})$ ,  $z \sim \mathcal{N}(0, 1)$ , and fixed our approximate posterior to be  $q(z|x) = \mathcal{N}(0, 1.5^2)$ . Unless otherwise specified, we employ the uniform partition strategy for both TVO and HBO. Observations from real data are characteristically similar to this toy.

**Bound sharpness** is the primary concern of this study. We compare the tightness of TVO, HBO and other competing variational bounds under various parameter configurations (partition number  $K$ , batch-size  $B$ , curvature  $\alpha$ , etc.). In Figure 5, we visualize the different popular bounds with matched configurations ( $K = 100, B = 10, \alpha = 0.8$ ), along with the true likelihood  $p(x)$ . We see HBO consistently provides a tighter approximation relative to its counterparts. In Figure 6 we plot the approximation error  $e(\hat{p}) = \int p(x)|p(x) - \hat{p}(x)| dx$  under different practical computational budgets, showing HBO significantly improves over TVO given the same budget. Note however, a sharper bound alone does not necessarily imply a better objective for variational learning (Rainforth et al., 2017). In the next experiment we examine other aspects that matter for a good variational objective.

**Estimation variance and effective sample size** are two factors that greatly affect the learning efficiency of VI. Low-variance estimators generally directly promote fast convergence (Mnih and Rezende,

2016; Jang et al., 2018; Roeder et al., 2017; Tucker et al., 2018); and the *effective sample-size* (ESS), or sample efficiency, describes on average how much does an individual sample contribute (Liu and Liu, 2001). For a weighted representation, the normalized ESS is defined as  $ESS \triangleq \frac{\sum_i \tilde{w}_i}{m \sum_i \tilde{w}_i^2} \in [\frac{1}{m}, 1]$ , where  $\{\tilde{w}_i\}$  denote the unnormalized weights and  $m$  is the original sample size. For a small ESS, only a small fraction of the samples are contributing; while for  $ESS = 1$ , each sample contributes equally.

Figure 7 compares the estimation variance and ESS along the thermodynamic path for TVO and its much flatter counterpart HBO. An interesting observation is that the variance shoots up when thermodynamic curves encounter a higher curvature. This partly explains why the original TVO is less competitive, as the partition points are mostly placed in the high-variance regions (small  $\beta$ ). While the sample efficiency achieves its maximum at the ELBO ( $\beta = 0$ ), it undergoes a sharp drop as we move along the TVO curve. HBO shows more robustness against the deterioration in sample efficiency and a much better variance profile in the low-temperature regime. In Figure S11, we compare averaged ESS of difference VI bounds on the real-world MNIST data. Our finding suggests smarter partition strategies should account for both variance and ESS to strike a better deal for the bias-variance trade-off in the design of empirical estimators.

**Matching complex posterior distributions.** We hypothesized that thermodynamic schemes did not outperform regular objectives because they only test simple posterior approximations. As such, we consider the more challenging case:  $y = \sqrt{z_1^2 + z_2^2} + \xi$ ,  $z_1, z_2 \sim \mathcal{N}(0, 1)$ ,  $\xi \sim \mathcal{N}(0, 0.1^2)$ , and the goal is to infer pair  $(z_1, z_2)$  given an observation  $y = 1$ , whose posterior will be highly nonlinear (see Figure S1). To model such complex posterior distribution, we use the *masked auto-regression flow* (MAF) (Papamakarios et al., 2017) to model the approximate posterior. We observe that neither ELBO nor IW-ELBO converged (Figure S1). Both thermodynamic schemes give reasonable approximations, but HBO converges slightly faster and to a better solution.

<sup>4</sup>Our code: [https://github.com/author\\_name/HBO](https://github.com/author_name/HBO)

TABLE 1: MNIST & OMNIGLOT RESULTS ( $\uparrow$  IS BETTER)

TEST	MNIST		OMNIGLOT	
	ELBO $\uparrow$	IW-ELBO $\uparrow$	ELBO $\uparrow$	IW-ELBO $\uparrow$
ELBO	-94.00	-89.34	-117.81	-108.12
IW-ELBO	-96.65	-88.31	-118.78	-108.13
RÉNYI	-94.82	-88.55	-117.68	-107.89
TVO	-96.30	-88.27	-117.60	-107.88
HBO	<b>-93.12</b>	<b>-87.82</b>	<b>-116.86</b>	<b>-107.70</b>

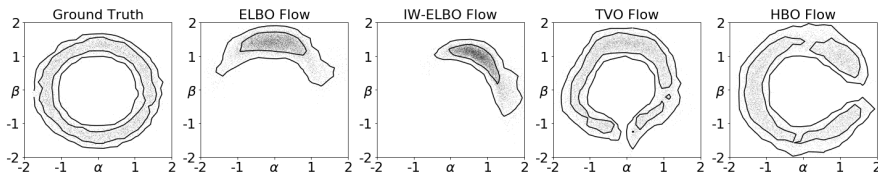


Figure 10: Posterior approximation with masked auto-regressive flows.

**Bayesian regression.** We also benchmark HBO’s performance against other bounds using the Bayesian regression model:  $Y = \alpha + \beta\tilde{X} + \epsilon$ ,  $X = \tilde{X} + \zeta$ ,  $p(\alpha, \beta) \propto (1 + \beta^2)^{-3/2}$ ,  $p(\sigma) \propto \frac{1}{\sigma}$  (details in SM Sec. E). We examine the convergence of different VI criteria quantitatively using the *maximal mean discrepancy* (MMD) metric (Gretton et al., 2012) to evaluate the similarity between the ground-truth posterior (computed from the `emcee` package) to the variational approximations. In Figure 11, we see HBO delivers the fastest convergence to ground-truth, followed by TVO and then IW-ELBO. Vanilla ELBO struggles the most. This is consistent with the theoretical predictions of the tightness of the bounds.

## 5.2 Real-world data

To demonstrate HBO’s ability to model real-world complex distributions, we consider analyzing the MNIST data in the main text, with details on implementation along with analyses for other popular benchmark datasets deferred to the SM Sec. D.

**Approximation quality.** Two aspects of VI approximation are of particular interest: (i) inference: the quality of the approximate posterior  $q_\phi(\mathbf{z}|\mathbf{x})$ ; and (ii) model: the quality of the likelihood approximation  $\log p_\theta(x)$ . (i) is particularly important, as many applications leverage VI as a principled probabilistic approach for representation extraction, which seeks high-quality encoders  $q_\phi(\mathbf{z}|\mathbf{x})$ .

These two aspects can be respectively assessed through the ELBO and IW-ELBO bounds, with the latter using large importance samples to accurately approximate the marginal log-likelihood. In Figure 9, we plot the evolution trajectories of respective bounds on the test set for the models trained with different variational objectives, with the numbers summarized in Table 1. Consistent with the analysis from Rainforth

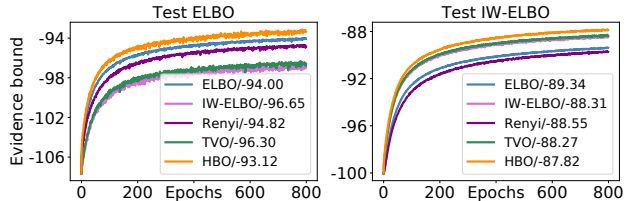


Figure 9: MNIST results on test data.

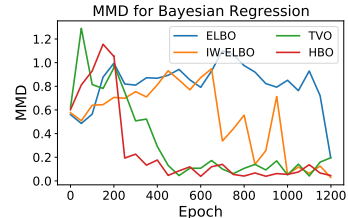


Figure 11: Posterior convergence for different bounds.

et al. (2017), ELBO trains better encoder compared with IW-ELBO and Rényi, but does worse in likelihood learning. Our new thermodynamic HBO scheme is immune to this tension, and performs better than competing solutions in both metrics.

**$\alpha$ -tuning, ablation and additional analyses.** Choosing the right  $\alpha$  is crucial for HBO. We applied the simple heuristic search procedure described in Section 3.3, with  $\alpha$  updated each epoch. It brings neglectable extra computations, while substantially improves performance (see ablation in the SM Sec. F). This distincts from Rényi and other parameterized variational objectives, where there is no good heuristics for parameter tuning. Limited by space, we provide extended ablations, analyses and results in the SM Sec. E-F, further assessing HBO’s inference and modeling properties, along with more real-world applications for image generation, language modeling and Bayesian regressions.

## 6 Conclusions

This study provides a comprehensive discussion of the recently introduced thermodynamic variational schemes. In particular, we elucidate the role of thermodynamic variational objectives in the larger picture of the modern VI literature. Motivated from a geometric argument, we present HBO, a novel generalization of thermodynamic variational bound that further improves TVO. Via seeking an alternative integration path, HBO flattens the pathological curve of local evidence, yielding a tighter bound. We also cover important topics such as automated parameter tuning. Empirical evidence verified that HBO enjoys low variance and high effective-sample size, leading to improved performance.

## References

- Arjovsky, M. and Bottou, L. (2017). Towards principled methods for training generative adversarial networks. In *NIPS Workshop*.
- Arjovsky, M., Chintala, S., and Bottou, L. (2017). Wasserstein generative adversarial networks. In *ICML*.
- Bamler, R., Zhang, C., Opper, M., and Mandt, S. (2017). Perturbative black box variational inference. In *NIPS*.
- Blei, D. M., Kucukelbir, A., and McAuliffe, J. D. (2017). Variational inference: A review for statisticians. *Journal of the American Statistical Association*, 112(518):859–877.
- Blei, D. M., Ng, A. Y., and Jordan, M. I. (2003). Latent Dirichlet allocation. *Journal of Machine Learning Research*, 3(Jan):993–1022.
- Brekelmans, R., Masrani, V., Wood, F., Steeg, G. V., and Galstyan, A. (2020). All in the exponential family: Bregman duality in thermodynamic variational inference. In *ICML*.
- Burda, Y., Grosse, R., and Salakhutdinov, R. (2016). Importance weighted autoencoders. In *ICLR*.
- Chen, J., Gan, Z., Li, X., Guo, Q., Chen, L., Gao, S., Chung, T., Xu, Y., Zeng, B., Lu, W., et al. (2021a). Simpler, faster, stronger: Breaking the log-k curse on contrastive learners with flatnce. *arXiv preprint arXiv:2107.01152*.
- Chen, J., Wang, S., Carin, L., and Tao, C. (2021b). Finite-time consensus learning for decentralized optimization with nonlinear gossiping. *arXiv preprint arXiv:2111.02949*.
- Chen, J., Xiu, Z., Henao, R., Goldstein, B., Carin, L., and Tao, C. (2020). Supercharging imbalanced data learning with energy-based contrastive representation transfer. *NeurIPS*.
- Crooks, G. E. (1999). Entropy production fluctuation theorem and the nonequilibrium work relation for free energy differences. *Physical Review E*, 60(3):2721.
- Dai, B., Dai, H., He, N., Liu, W., Liu, Z., Chen, J., Xiao, L., and Song, L. (2018). Coupled variational bayes via optimization embedding. In *NeurIPS*, pages 9712–9722.
- Dempster, A. P., Laird, N. M., and Rubin, D. B. (1977). Maximum likelihood from incomplete data via the em algorithm. *Journal of the Royal Statistical Society: Series B (Methodological)*, 39(1):1–22.
- Dieng, A. B., Tran, D., Ranganath, R., Paisley, J., and Blei, D. M. (2017). Variational inference via chi upper bound minimization. In *NIPS*.
- Dinh, L., Sohl-Dickstein, J., and Bengio, S. (2016). Density estimation using real nvp. *arXiv preprint arXiv:1605.08803*.
- Du, Y. and Mordatch, I. (2019). Implicit generation and modeling with energy based models. In *NeurIPS*, pages 3603–3613.
- Dumoulin, V., Belghazi, I., Poole, B., Mastropietro, O., Lamb, A., Arjovsky, M., and Courville, A. (2016). Adversarially learned inference. *arXiv preprint arXiv:1606.00704*.
- Durkan, C., Bekasov, A., Murray, I., and Papamakarios, G. (2019). Neural spline flows. *arXiv preprint arXiv:1906.04032*.
- Frenkel, D. and Smit, B. (2001). *Understanding molecular simulation: from algorithms to applications*, volume 1. Elsevier.
- Friston, K., Mattout, J., Trujillo-Barreto, N., Ashburner, J., and Penny, W. (2007). Variational free energy and the laplace approximation. *NeuroImage*, 34(1):220–234.
- Gelman, A. and Meng, X.-L. (1998). Simulating normalizing constants: From importance sampling to bridge sampling to path sampling. *Statistical science*, pages 163–185.
- Geyer, C. J. (1991). Markov chain Monte Carlo maximum likelihood.
- Geyer, C. J. (1994). On the convergence of monte carlo maximum likelihood calculations. *Journal of the Royal Statistical Society. Series B (Methodological)*, pages 261–274.
- Goodfellow, I., Pouget-Abadie, J., Mirza, M., Xu, B., Warde-Farley, D., Ozair, S., Courville, A., and Bengio, Y. (2014). Generative adversarial nets. In *NIPS*.
- Gregor, K., Danihelka, I., Graves, A., Rezende, D. J., and Wierstra, D. (2015). Draw: A recurrent neural network for image generation. In *ICML*.
- Gretton, A., Borgwardt, K. M., Rasch, M. J., Schölkopf, B., and Smola, A. (2012). A kernel two-sample test. *Journal of Machine Learning Research*, 13(Mar):723–773.
- Grosse, R. B., Maddison, C. J., and Salakhutdinov, R. R. (2013). Annealing between distributions by averaging moments. In *NIPS*.
- Gutmann, M. and Hirayama, J.-i. (2012). Bregman divergence as general framework to estimate unnormalized statistical models. *arXiv preprint arXiv:1202.3727*.
- Gutmann, M. and Hyvärinen, A. (2010). Noise-contrastive estimation: A new estimation principle for unnormalized statistical models. In *AISTATS*.

- Gutmann, M. U. and Hyvärinen, A. (2012). Noise-contrastive estimation of unnormalized statistical models, with applications to natural image statistics. *Journal of Machine Learning Research*, 13(Feb):307–361.
- Habeck, M. (2012). Evaluation of marginal likelihoods via the density of states. In *AISTATS*.
- Habeck, M. (2017). Model evidence from nonequilibrium simulations. In *NIPS*.
- Hernández-Lobato, J. M., Li, Y., Rowland, M., Hernández-Lobato, D., Bui, T., and Turner, R. (2016). Black-box  $\alpha$ -divergence minimization.
- Hinton, G. E. (2002). Training products of experts by minimizing contrastive divergence. *Neural Computation*, 14(8):1771–1800.
- Hoffman, M. D., Blei, D. M., Wang, C., and Paisley, J. (2013). Stochastic variational inference. *The Journal of Machine Learning Research*, 14(1):1303–1347.
- Hyvärinen, A. (2005). Estimation of non-normalized statistical models by score matching. *Journal of Machine Learning Research*, 6(Apr):695–709.
- Jang, E., Gu, S., and Poole, B. (2018). Categorical reparameterization with gumbel-softmax. In *AISTATS*.
- Kingma, D. P. and Dhariwal, P. (2018). Glow: Generative flow with invertible 1x1 convolutions. In *Advances in Neural Information Processing Systems*, pages 10215–10224.
- Kingma, D. P., Salimans, T., and Welling, M. (2016). Improving variational inference with inverse autoregressive flow. In *NIPS*.
- Kingma, D. P. and Welling, M. (2014). Auto-encoding variational Bayes. In *ICLR*.
- Krizhevsky, A., Hinton, G., et al. (2009). Learning multiple layers of features from tiny images.
- Lake, B. M., Salakhutdinov, R., and Tenenbaum, J. B. (2015). Human-level concept learning through probabilistic program induction. *Science*, 350(6266):1332–1338.
- Lartillot, N. and Philippe, H. (2006). Computing bayes factors using thermodynamic integration. *Systematic biology*, 55(2):195–207.
- Li, Y. and Turner, R. E. (2016). Rényi divergence variational inference. In *NIPS*.
- Lindsay, B. G. (1995). Mixture models: theory, geometry and applications. In *NSF-CBMS regional conference series in probability and statistics*, pages i–163. JSTOR.
- Liu, J. S. and Liu, J. S. (2001). *Monte Carlo strategies in scientific computing*, volume 10. Springer.
- Liu, Q. and Wang, D. (2016). Stein variational gradient descent: A general purpose bayesian inference algorithm. In *NIPS*.
- Liu, Z., Luo, P., Wang, X., and Tang, X. (2018). Large-scale celebfaces attributes (celeba) dataset. Retrieved August, 15(2018):11.
- Lu, D., Tao, C., Chen, J., Li, F., Guo, F., and Carin, L. (2020). Reconsidering generative objectives for counterfactual reasoning. In *NeurIPS*.
- Maaløe, L., Sønderby, C. K., Sønderby, S. K., and Winther, O. (2016). Auxiliary deep generative models. In *ICML*.
- Masrani, V., Brekelmans, R., Bui, T., Nielsen, F., Galstyan, A., Steeg, G. V., and Wood, F. (2021). q-paths: Generalizing the geometric annealing path using power means. In *UAI*.
- Masrani, V., Le, T. A., and Wood, F. (2019). The thermodynamic variational objective. In *NeurIPS*.
- Mescheder, L., Nowozin, S., and Geiger, A. (2017). Adversarial variational Bayes: unifying variational autoencoders and generative adversarial networks. In *ICML*.
- Miller, A. C., Foti, N., and Adams, R. P. (2016). Variational boosting: Iteratively refining posterior approximations. In *ICML*.
- Minka, T. P. (2013). Expectation propagation for approximate bayesian inference. *arXiv preprint arXiv:1301.2294*.
- Mnih, A. and Rezende, D. J. (2016). Variational inference for monte carlo objectives. In *ICML*.
- Mohamed, S. and Lakshminarayanan, B. (2016). Learning in implicit generative models. *arXiv preprint arXiv:1610.03483*.
- Müller, A. (1997). Integral probability metrics and their generating classes of functions. *Advances in Applied Probability*, 29(2):429–443.
- Neal, R. M. (2001). Annealed importance sampling. *Statistics and computing*, 11(2):125–139.
- Nijkamp, E., Hill, M., Zhu, S.-C., and Wu, Y. N. (2019). Learning non-convergent non-persistent short-run MCMC toward energy-based model. In *NeurIPS*, pages 5233–5243.
- Nowozin, S., Cseke, B., and Tomioka, R. (2016). f-GAN: Training generative neural samplers using variational divergence minimization. In *NIPS*.
- Ogata, Y. (1989). A monte carlo method for high dimensional integration. *Numerische Mathematik*, 55(2):137–157.
- Oord, A. v. d., Li, Y., Babuschkin, I., Simonyan, K., Vinyals, O., Kavukcuoglu, K., Driessche, G. v. d.,



- Lockhart, E., Cobo, L. C., Stimberg, F., et al. (2017). Parallel wavenet: Fast high-fidelity speech synthesis. *arXiv preprint arXiv:1711.10433*.
- Ozair, S., Lynch, C., Bengio, Y., Oord, A. v. d., Levine, S., and Sermanet, P. (2019). Wasserstein dependency measure for representation learning. *NeurIPS*.
- Papamakarios, G., Nalisnick, E., Rezende, D. J., Mohamed, S., and Lakshminarayanan, B. (2019). Normalizing flows for probabilistic modeling and inference. *arXiv preprint arXiv:1912.02762*.
- Papamakarios, G., Pavlakou, T., and Murray, I. (2017). Masked autoregressive flow for density estimation. In *NIPS*.
- Parzen, E. (1962). On estimation of a probability density function and mode. *The annals of mathematical statistics*, 33(3):1065–1076.
- Pu, Y., Gan, Z., Henao, R., Li, C., Han, S., and Carin, L. (2017). VAE learning via Stein variational gradient descent. In *NIPS*.
- Rainforth, T., Le, T. A., Maddison, M. I. C. J., and Wood, Y. W. T. F. (2017). Tighter variational bounds are not necessarily better. In *NIPS workshop*.
- Ranganath, R., Gerrish, S., and Blei, D. (2014). Black box variational inference. In *AISTATS*.
- Ranganath, R., Tran, D., and Blei, D. (2016). Hierarchical variational models. In *ICML*.
- Rényi, A. et al. (1961). On measures of entropy and information. In *Proceedings of the Fourth Berkeley Symposium on Mathematical Statistics and Probability, Volume 1: Contributions to the Theory of Statistics*. The Regents of the University of California.
- Rezende, D. J. and Mohamed, S. (2015). Variational inference with normalizing flows. In *ICML*.
- Roeder, G., Wu, Y., and Duvenaud, D. K. (2017). Sticking the landing: Simple, lower-variance gradient estimators for variational inference. In *NIPS*.
- Salimans, T., Kingma, D., and Welling, M. (2015). Markov chain Monte Carlo and variational inference: Bridging the gap. In *International Conference on Machine Learning*.
- Shen, T., Lei, T., Barzilay, R., and Jaakkola, T. (2017). Style transfer from non-parallel text by cross-alignment.
- Sriperumbudur, B. K., Fukumizu, K., Gretton, A., Schölkopf, B., and Lanckriet, G. R. (2009). On integral probability metrics,  $\phi$ -divergences and binary classification. *arXiv preprint arXiv:0901.2698*.
- Tao, C., Chen, L., Dai, S., Chen, J., Bai, K., Wang, D., Feng, J., Lu, W., Bobashev, G., and Carin, L. (2019a). On fenchel mini-max learning. In *NeurIPS*.
- Tao, C., Chen, L., Zhang, R., Henao, R., and Duke, L. C. (2018). Variational inference and model selection with generalized evidence bounds. In *ICML*.
- Tao, C., Dai, S., Chen, L., Bai, K., Chen, J., Liu, C., Zhang, R., Bobashev, G., and Duke, L. C. (2019b). Variational annealing of gans: A langevin perspective. In *ICML*, pages 6176–6185. PMLR.
- Tomczak, J. and Welling, M. (2018). VAE with a VampPrior. In *AISTATS*.
- Tucker, G., Lawson, D., Gu, S., and Maddison, C. J. (2018). Doubly reparameterized gradient estimators for monte carlo objectives. *arXiv preprint arXiv:1810.04152*.
- Wan, N., Li, D., and Hovakimyan, N. (2020).  $f$ -divergence variational inference. *Advances in Neural Information Processing Systems*, 33.
- Williams, R. J. (1992). Simple statistical gradient-following algorithms for connectionist reinforcement learning. *Machine learning*, 8(3-4):229–256.
- Wu, Y., Burda, Y., Salakhutdinov, R., and Grosse, R. (2017). On the quantitative analysis of decoder-based generative models. In *ICLR*.
- Yang, Z., Hu, Z., Salakhutdinov, R., and Berg-Kirkpatrick, T. (2017). Improved variational autoencoders for text modeling using dilated convolutions. In *ICML*, pages 3881–3890. PMLR.

# Appendix

## Table of Contents

---

<b>A</b>	<b>Extended Results and Discussions</b>	<b>13</b>
A.1	Statement . . . . .	13
A.2	When do TVO/HBO bounds work better? . . . . .	13
A.3	Mode covering behavior . . . . .	13
A.4	More related work . . . . .	16
<b>B</b>	<b>Figures Cited in the Main Text</b>	<b>18</b>
<b>C</b>	<b>Technical Proofs and Derivations</b>	<b>18</b>
C.1	Proof of Proposition 2.1 (Equivalence to the Rényi Bound) . . . . .	18
C.2	Proof of Proposition 3.1 (Wasserstein Thermodynamic Bounds) . . . . .	19
C.3	Proof of Proposition 3.3 (Monotonicity of HBO) . . . . .	21
C.4	Derivation for the Importance Weighted HBO . . . . .	21
C.5	Derivation for the Perturbed HBO Estimator . . . . .	22
<b>D</b>	<b>Experimental Setups</b>	<b>24</b>
D.1	Datasets . . . . .	24
D.2	Numerical integration . . . . .	24
D.3	Model architectures (standard) . . . . .	24
D.4	Inference with normalizing flows . . . . .	25
D.5	Baselines and specifications . . . . .	25
<b>E</b>	<b>Additional Results and Analyses for Synthetic Examples</b>	<b>25</b>
E.1	Bayesian regression . . . . .	25
E.2	Bayesian inference for complex posterior . . . . .	26
<b>F</b>	<b>Additional Results and Analyses for Real-World Datasets</b>	<b>28</b>

---

## A Extended Results and Discussions

### A.1 Statement

The author(s) would like to note that this work was originally prepared back in late 2019 titled “*Flattening The Curve: Variational Inference with Hölder Bound*”. When it was first submitted for review in early 2020, the global pandemic hits. The reviewers had concerns the phrase “flattening the curve” may be considered implicitly referencing the on-going raging pandemic and would inadvertently jog sorrow memories. This was not the case since this study was complete work before COVID (8-page main text with 11-page Appendix, excluding refs). That said, the author(s) understood this concern and decided to change the title, withdraw submission and wait until COVID pandemic recedes to resubmit this work. The earliest appearance of other work with a similar idea appear only in late 2020, and only as a 4-pager workshop submission with only toy experiments.

### A.2 When do TVO/HBO bounds work better?

Despite their elegant formulation, the family of thermodynamic variational objectives, such as the original TVO and the proposed HBO, has been critically challenged for its practical utility. As the original TVO paper has observed (Masrani et al., 2019), TVO offers similar performance relative to IW-ELBO. We devote this section to clarify why people fail to benefit from the supposedly-exact TVO-type bounds, and provide concrete examples where TVOs learns efficiently while other more standard variational bounds struggle.

In the main text, we have provided arguments based on estimation variance and effective sample size to support HBO and TVO. However, these two alone can not guarantee TVOs work better than the other alternatives. Here we want to offer some additional insights.

We argue the key lies in the gap between: (a) the complexity of posterior distribution  $p_\theta(z|x)$ ; (b) the expressive power of the posterior approximator  $q_\phi(z|x)$ . Our observation is that, TVO-type variational objectives are mostly handicapped by the expressive power of  $q_\phi(z|x)$ , which typically takes the convenient choice of mean-field Gaussian distributions in practice. When the ground-truth posterior distribution shows apparent deviations from Gaussianity, the Gaussian posterior approximations learned by alternative variational bounds are not characteristically different.

To make this point clear, let us look at the Bayesian inference example described in Sec E.2. In this example, the true posterior is approximately a unit circle (Figure S1). With Gaussian approximation, the estimated parameter distribution only covers a corner of the circle. Of course one can conveniently blame this on a bad choice of  $q_\phi(z|x)$ , and thinks the true-posterior can be recovered by using a more flexible posterior, say *normalizing flows* (Rezende and Mohamed, 2015). Unfortunately, that is not the case. In Figure S2 and Figure S3, we show that even one adopts a highly-expressive non-parametric normalizing flow (see Sec D.4), using ELBO and IW-ELBO objectives do not adequately approximate the true posterior. Encouragingly, we see good convergence to the ground-truth for TVO-type objectives (Figure S4 and Figure S5). Between the two, HBO converges a little bit faster. In Sec E we will further confirm these observations quantitatively using other distributional metric. Based on experiment evidence, this better convergence might result from the mode-covering behavior of HBO (see below).

### A.3 Mode covering behavior

For Bayesian inference, one might be interested in the mode covering behavior of an estimator: whether the estimated posterior is condensed in the high-density region of the true posterior (*i.e.*, mode-seeking), or it covers up the support of the true posterior (*i.e.*, mode-covering). Different applications might desire different mode covering behaviors (Li and Turner, 2016; Dieng et al., 2017). Our experiments seem to suggest overall HBO favors covering the true posterior distribution (see for instance, Figure S10).

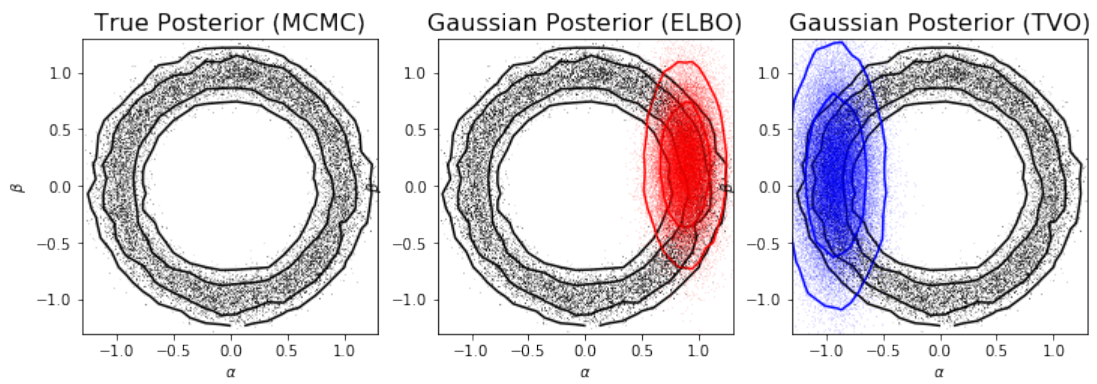


Figure S1: True posterior (left) and Gaussian variational approximations (through ELBO and TVO).

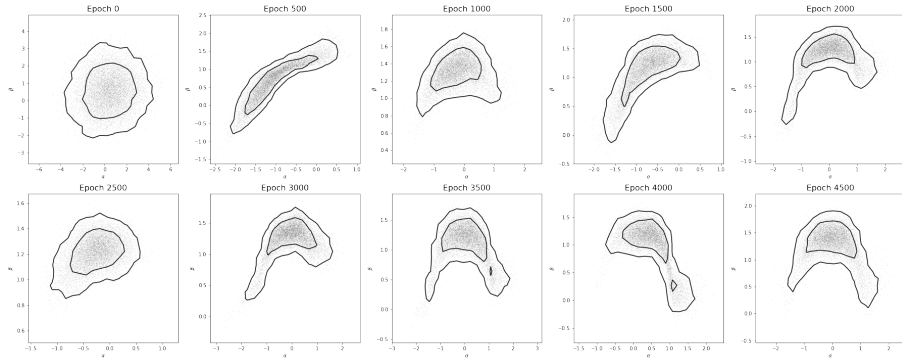


Figure S2: Flow-posterior trained with ELBO, **unable to converge**.

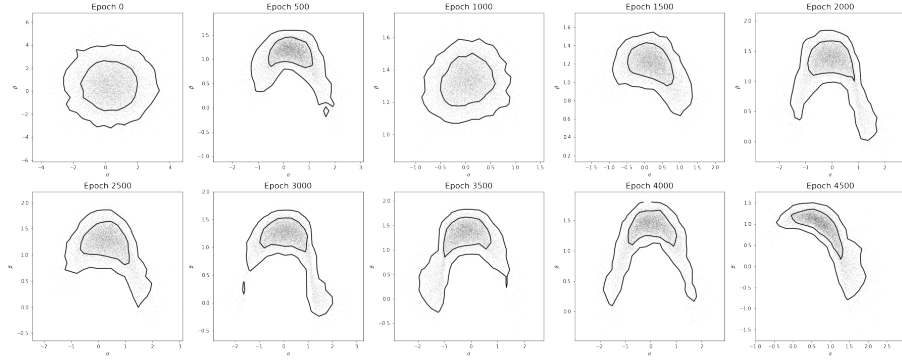


Figure S3: Flow-posterior trained with IW-ELBO( $S = 5$ ), **unable to converge**.

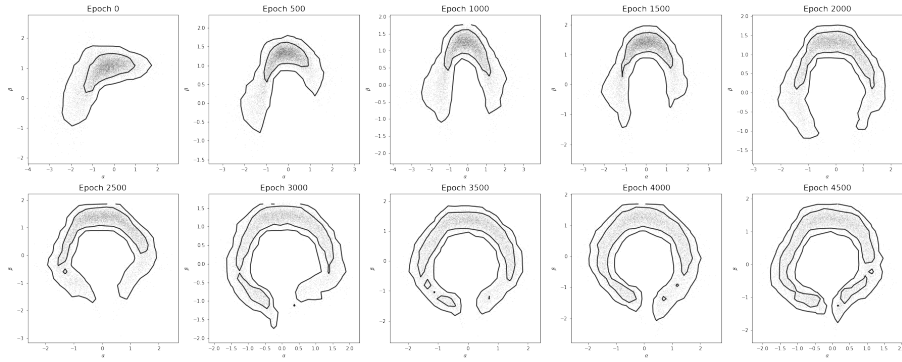


Figure S4: Flow-posterior trained with TVO( $S = 5, K = 5$ ), **converge**.

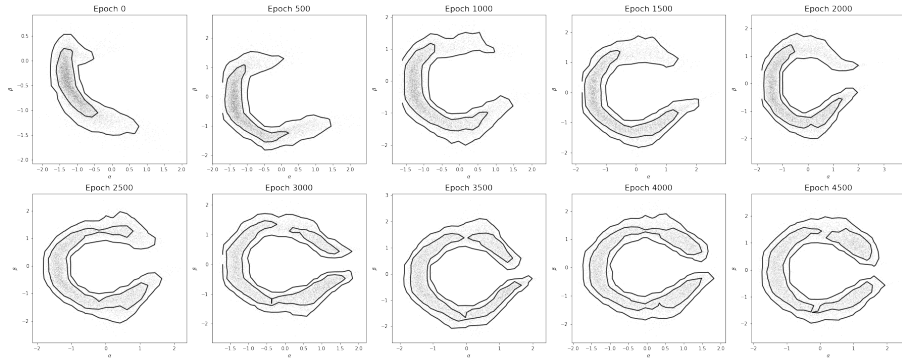


Figure S5: Flow-posterior trained with HBO( $\alpha = 10^{-3}, S = 5, K = 5$ ), **converge**.

#### A.4 More related work

**Likelihood estimation** has been a long-standing challenge for both statistical and machine learning communities. Classical solutions, such as kernel density estimation Parzen (1962) and mixture models Lindsay (1995), does not scale-well with the dimensionality and complexity of modern datasets, such as images and natural languages. For machine learning applications, usually there are a few additional expectations for a “good” likelihood estimation procedure: it is *generative*, in the sense that samples can be easily drawn from the learned model Mohamed and Lakshminarayanan (2016); Nowozin et al. (2016); it is *recapitulative*, such that it summarizes the important features of the data that can be repurposed Dumoulin et al. (2016).

Recent advances focused on both modeling flexibility and computational scalability of likelihood-based learning procedures, and can be broadly categorized into *exact-likelihood* models and *approximate inference* models. The exact-likelihood models progressively build up complex distributions via stacking simple transformations with easy-to-compute Jacobians Dinh et al. (2016), and thus commonly being referenced to as *flow-based* models Rezende and Mohamed (2015); Kingma et al. (2016); Kingma and Dhariwal (2018). While proven quite powerful, they are excessively resource demanding and often requires dedicated engineering efforts for large-scale problems Oord et al. (2017), and consequently limiting their direct application in practical terms. Note that flow-based procedures have been successfully applied to improve the expressiveness of the approximate posterior in VI, and marry it to our HBO may yield additional gains.

**Approximate inference** models, like their name suggest, seek to efficiently optimize cheap approximations to the likelihood, which includes procedures such as *expectation maximization* (EM) Dempster et al. (1977), *expectation propagation* (EP) Minka (2013) and *variational inference* (VI) (see Hernández-Lobato et al. (2016) for a unifying perspective). In recent years, VI, more commonly known under the name *variational auto-encoder* (VAE) in the machine learning context Kingma and Welling (2014), gained its popularity due to its easy implementation, intuitive interpretation, strong performance and versatility in its presentations. As discussed in the main text, (i) tightening the variational gap and (ii) reducing variance construct two main research topics in VI. As we have shown, via properly tuning the geometry parameter  $\alpha$ , the proposed HBO improves both aspects: it allows sharp approximation with low computational budget <sup>5</sup>, and it empirically shows low variance and high sample efficiency.

Note that variants of VI which does not necessarily conform to the likelihood perspective, such as  $\beta$ -VAE and adversarial auto-encoder (AAE), have been proven most useful in practice (assessed using domain-specific metrics in addition to the likelihood). These attempts can be sometimes interpreted as empirical adjustments to correct for the modeling bias due to misspecification. How, and will the integration of HBO perspectives lend additional benefits provide an interesting topic for future investigation.

Close to HBO is the work of GLBO Tao et al. (2018), which shared a number of motivations. GLBO also sets off its discussion from a geometrical argument. Unlike HBO, GLBO decomposes variational objectives into a composition of convex map and its inverse, interlaced with the expectation of the approximate posterior. A keen observation of GLBO is that, via altering the geometry of the convex transform, making it “flatter”, results in tighter bounds, at the price of a higher variance. Compared to GLBO, our HBO considers flattening in the thermodynamic domain, and does not pay the price for the exacerbated variance. The GLBO paper also discussed the perturbed estimator and shared insights on model selection for VI, which inspires similar efforts in our development.

**Alternative distribution discrepancy metrics** with appealing characteristics compared to the KL-divergence minimization criteria implicitly assumed by the likelihood-based learning, have been extensively studied in machine learning. Such efforts include direct generalizations to the *information theoretic divergence*, also known as the *f-divergence*. An interesting intersection with the current study is the Rényi VI, where the variational gap being optimized is the  $\alpha$ -divergence. Li and Turner (2016) discussed different profiles of the approximate posterior learned with Rényi VI objectives, and our analysis shows its connection to TVO. Note that a major criticism against the information theoretic measures is that they are not metric-aware Arjovsky and Bottou (2017); Ozair et al. (2019). In other words, small perturbations to the distribution can result in drastic changes in the *f-divergence*. Such undefined behavior can be overcome by the *integral probability metrics* (IPM)

<sup>5</sup>The savings would be tremendous if one need to sample exactly from the intermediate distribution rather than appealing to importance reweighting.



Müller (1997); Sriperumbudur et al. (2009), including prominent examples such as *maximal mean discrepancy* (MMD) Gretton et al. (2012) and *Wasserstein distance* Arjovsky et al. (2017). IPM is defined as the maximal contrast between two distributions wrt a fixed function space. And via a Kantorovich-Rubinstein duality argument, it can be shown that with an appropriate choice of function space, IPM can be expressed in terms of the distance given by the ground metric. This motivates the development of both primal and dual solver for IPM distance.

**Adversarial schemes** have recently demonstrated their effectiveness in handling complex, intractable distributions Goodfellow et al. (2014). Their applications have been previously considered for the improvement of VI, such as *adversarial variational Bayes* (AVB) Mescheder et al. (2017), *coupled variational inference* (CVB) Dai et al. (2018) and Fenchel mini-max VAE Tao et al. (2019a). While a direct generalization of such schemes to HBO is straightforward, we caution extra care must be taken, as the thermodynamic integration may be sensitive to the approximation error of the likelihood contrast.

**The utility and tightness trade-off** for the variational posterior is first formally investigated in Rainforth et al. (2017). Intuitively, it says with a sharper variational bound to the marginal likelihood, the optimization procedure is less incentivized to improve the variational posterior  $q_\phi(\mathbf{z}|\mathbf{x})$ . Our analysis suggests that thermodynamic objectives, such as HBO, might be immune to this dilemma. And a plausible explanation is offered: in HBO, posterior samples contribute more “equally”.

**Automated tuning** is an important yet less studied topic in the VI context. It promises to alleviate the burden of model fitting for empirical investigators and avoid introducing subjective bias. While the specific tuning target is tailored for HBO, some designing principles and experience can be shared. For one, the proposed HBO tuning explicitly seeks to minimize the variance along the thermodynamic curve. Also, our analysis the effective sample-size indicate alternative target for future improvements. Close to our developments is the adaptive TVO partition scheme, which replaces Riemannian integration with Lebesgue integration. Also in Tao et al. (2018); Lu et al. (2020) the authors explored maximal entropy principle for model selection in VI.

**More open questions** are in order following our HBO developments, which is beyond the scope of current study. A key question is under what conditions, if possible, can we ensure the monotonicity of the thermodynamic curve? This is significant as the monotonicity flipping point directly implies one-step approximation of the exact likelihood. Although in the absence of such analysis, one still hopes to considerably improve the performance of VI using the HBO perspectives. Practically, while our study characterize the qualitative behavior of HBO, there is much room for quantitative improvements. Like all predecessors of thermodynamic inference procedures, our results do not see a drastic boost relative to the existing counterparts, possibly limited by the restrictive modeling choices we have adopted (*e.g.*, MLP architecture and Gaussian posterior). Potential improvements are expected using more expressive model architectures. Also of particular interest is whether there is a better alternative proposal sampler between the extremes of an MCMC sampler and the approximate posterior sampler.

**MCMC Variational Inference (Salimans et al., 2015)** belongs to a more general family of VI schemes known as the *Auxiliary VI* (Aux-VI) (Maaløe et al., 2016), which seeks to improve bound sharpness via introducing auxiliary latent variables  $\tilde{z}$ . Standard ELBO employs  $q(z|x)$  with simple forms that enjoy analytical expressions (*e.g.*, mean field Gaussian), which limits the expressive power of the posterior and subsequently compromises sharpness. To overcome this limitation, Aux-VI assumes an augmented latent variable model  $p_\theta^\dagger(x, z, \tilde{z}) = p_\theta(x, z)r_\theta(\tilde{z}|x, z)$  and variational posterior  $q_\phi^\dagger(z, \tilde{z}|x) = q_\phi^\dagger(z|x, \tilde{z})q_\phi^\dagger(\tilde{z}|x)$ , denoting

$$\begin{aligned} \text{VI}_{\text{Aux}} &\triangleq \mathbb{E}_{Z, \tilde{Z} \sim q_\phi^\dagger} \left[ \log \frac{p_\theta^\dagger(x, Z, \tilde{Z})}{q_\phi^\dagger(Z, \tilde{Z}|x)} \right], \\ \text{ELBO}^\dagger &\triangleq \mathbb{E}_{Z \sim q_\phi^\dagger} \left[ \log \frac{p_\theta^\dagger(x, Z)}{q_\phi^\dagger(Z|x)} \right], \end{aligned} \tag{19}$$

where we have used  $\text{ELBO}^\dagger$  to differentiate the auxiliary latent-augmented ELBO from the vanilla ELBO. One may readily verify that

$$\text{VI}_{\text{Aux}} = \text{ELBO}^\dagger - \bar{\mathbb{D}}_{\text{KL}} \leq \text{ELBO}^\dagger \leq \log p_\theta(x), \tag{20}$$

where  $\bar{\mathbb{D}}_{\text{KL}} \triangleq \mathbb{E}_{Z \sim q_\phi^\dagger(z|x)} \left[ \text{KL}(q_\phi^\dagger(\tilde{z}|x, Z) \parallel p_\theta(\tilde{z}|x, Z)) \right]$ . Note  $\tilde{z}$  is typically defined by a sequence of simple transition kernels  $q(\tilde{z}_{t+1}|\tilde{z}_t, x)$  for tractable computations. Here  $\text{VI}_{\text{Aux}}$  is to be compared with standard ELBO defined by  $q(z|x)$ . The motivation behind Aux-VI is that, since the marginalized latent distribution  $q_\phi^\dagger(z|x) \triangleq \mathbb{E}_{\tilde{Z} \sim q(\tilde{z}|x)} [q(z, \tilde{Z}|x)]$  is very expressive, it is anticipated to bring more increases in the ELBO<sup>†</sup> term compared to the reductions from the  $\bar{\mathbb{D}}_{\text{KL}}$  term due to the auxiliary variables  $\tilde{z}$ , which means  $\text{ELBO} \leq \text{VI}_{\text{Aux}}$  is very likely to hold.

A concrete implementation of Aux-VI is the MCMC-VI formulated in Salimans et al. (2015), where the  $(z, \tilde{z})$  is specified in a hierarchical fashion using Markov chains, *i.e.*,

$$\begin{aligned} \tilde{z} &= [\tilde{z}_0, \dots, \tilde{z}_T], \quad z \triangleq \tilde{z}_T, \\ q_\phi^\dagger(\tilde{z}|x) &: \tilde{z}_t \sim q_t(\tilde{z}_t|x, \tilde{z}_{t-1}), \\ r_\theta(\tilde{z}|x, z) &: \tilde{z}_t \sim \tilde{r}_t(\tilde{z}_t|x, \tilde{z}_{t+1}), \end{aligned} \quad (21)$$

and here  $\{q_t, \tilde{r}_t\}_t$  denote the transition kernels. Hereafter we omit the dependence of approximate posterior  $q$  on data  $x$  for clarity. When each  $q_t(\tilde{z}_t|\tilde{z}_{t-1})$  observe the detailed balance for  $\pi_{\beta_t}$ , *i.e.*, the intermediates on the geometric path, and if the reverse model  $r(\tilde{z}_{t-1}|\tilde{z}_t) = q_t(\tilde{z}_t|\tilde{z}_{t-1})\pi_t(\tilde{z}_{t-1})/\pi_t(\tilde{z}_t)$ , one arrives at

$$\text{VI}_{\text{MCMC}} = \underbrace{\mathbb{E}_{\tilde{Z}_{1:T} \sim q(\tilde{z}|x)} \left[ \sum_t \Delta\beta_t \log \frac{p_\theta(x, \tilde{Z}_t)}{q_0(\tilde{Z}_t)} \right]}_{\text{TVO}}, \quad (22)$$

where  $\Delta\beta_t \triangleq (\beta_t - \beta_{t-1})$ . One can readily recognize that the  $\text{VI}_{\text{MCMC}}$  defined in (22) exactly recovers the TVO estimator. Note that the original MCMC-VI paper was unable to establish the tightness of its bound as  $\max\{\Delta\beta_t\} \rightarrow 0$ , a result that straightforward under the TVO framework.

## B Figures Cited in the Main Text

Figure S6 visualizes representative examples of Hölder paths, including special examples of geometric mean path ( $\alpha = 0$ ) and Wasserstein mean path ( $\alpha = 1$ ).

Figure S7 compares TVO bounds and HBO bounds with different partition budget with uniform partitioning. We set  $\alpha = 0.2$  in this case.

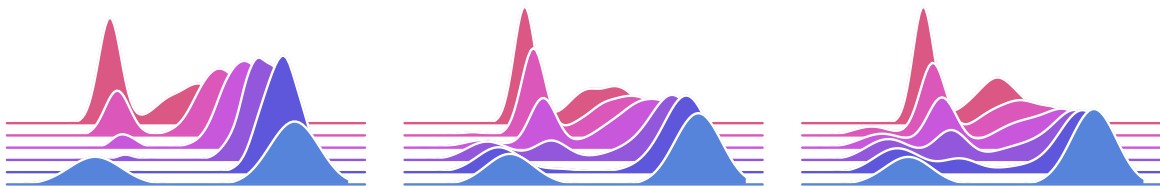


Figure S6: Comparison of different Hölder paths. From left to right:  $\alpha = 0, 0.5, 1$ , respectively for geometric mean path, Hölder mean path and Wasserstein mean path.

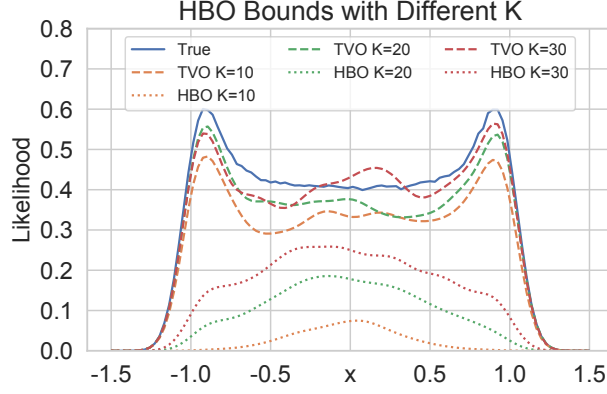
## C Technical Proofs and Derivations

In this section, we give details of the technical proofs and derivations for the results reported in the main text.

### C.1 Proof of Proposition 2.1 (Equivalence to the Rényi Bound)

**Definition S1.** Variational Rényi bound

$$\mathcal{L}_\alpha(\tilde{\pi}_1, \tilde{\pi}_0) = \frac{1}{\alpha} \log \mathbb{E}_{\pi_0} \left[ \left( \frac{\tilde{\pi}_1}{\tilde{\pi}_0} \right)^\alpha \right] \quad (23)$$


 Figure S7: Comparison of TVO and HBO bounds with different partition budget  $K$ .

**Proposition 2.1**  $\mathcal{L}_\alpha(\tilde{\pi}_1, \tilde{\pi}_0) = \frac{1}{\alpha} \int_0^\alpha \mathbb{E}_{\pi_{0,\beta}}[U'_{0,\beta}] d\beta$ .

*Proof.*

$$\mathcal{L}_\alpha(\tilde{\pi}_1, \tilde{\pi}_0) = \frac{1}{\alpha} \log \int \tilde{\pi}_1^\alpha(z) \tilde{\pi}_0^{1-\alpha}(z) dz = \frac{1}{\alpha} \log Z_{0,\alpha} = \frac{1}{\alpha} \int_0^\alpha \mathbb{E}_{\pi_{0,\beta}}[U'_{0,\beta}] d\beta \quad (24)$$

□

## C.2 Proof of Proposition 3.1 (Wasserstein Thermodynamic Bounds)

Recall Wasserstein thermodynamic path is given by the following family of intermediate distributions:

$$\tilde{\pi}_\beta^W = \beta \tilde{\pi}_1 + (1 - \beta) \tilde{\pi}_0, \quad Z_\beta^W = \int_{\mathcal{Z}} \tilde{\pi}_\beta^W(z) dz, \quad \pi_\beta^W = \frac{\tilde{\pi}_\beta^W}{Z_\beta^W}, \quad \beta \in [0, 1] \quad (25)$$

For sufficiently smooth  $\tilde{\pi}_\beta^W$  (e.g.,  $\tilde{\pi}^W$  and  $\log \tilde{\pi}^W$  are continuous wrt  $z$  and  $\beta$  both), we can exchange the integration with differentiation

$$\begin{aligned} \frac{\partial \log Z_\beta^W}{\partial \beta} &= \frac{1}{Z_\beta^W} \frac{\partial}{\partial \beta} Z_\beta^W = \frac{1}{Z_\beta^W} \frac{\partial}{\partial \beta} \int \tilde{\pi}_\beta^W dz \\ &= \int \frac{\tilde{\pi}_\beta^W}{Z_\beta^W} \frac{\partial}{\partial \beta} \log \tilde{\pi}_\beta^W dz = \mathbb{E}_{\pi_\beta^W} \left[ \frac{\partial}{\partial \beta} \log \tilde{\pi}_\beta^W \right] \end{aligned} \quad (26)$$

Denote  $U_\beta^W \triangleq \log \tilde{\pi}_\beta^W$ , we integrate out  $\beta$  on both sides of (26),

$$\int_0^1 \frac{\partial \log Z_\beta^W}{\partial \beta} d\beta = \int_0^1 \mathbb{E}_{Z \sim \pi_\beta^W} [\partial_\beta U_\beta^W(Z)] d\beta, \quad (27)$$

which gives

$$\log Z_1 - \log Z_0 = \int_0^1 \mathbb{E}_{Z \sim \pi_\beta^W} [U'_\beta(Z)] d\beta. \quad (28)$$

Denote the local evidence as

$$h(\beta) \triangleq \mathbb{E}_{\pi_\beta^W} \left[ \frac{\tilde{\pi}_1^W - \tilde{\pi}_0^W}{\tilde{\pi}_\beta^W} \right] \quad (29)$$

We want to show that  $h(\beta)$  is non-increasing.

*Proof.* For notational clarity, here we suppress the superscript  $W$  on the partition function  $Z_\beta$ .

$$\begin{aligned}
 \frac{\partial}{\partial \beta} h(\beta) &= \frac{\partial}{\partial \beta} \left[ \int \pi_\beta^W(z) \frac{\tilde{\pi}_1^W(z) - \tilde{\pi}_0^W(z)}{\tilde{\pi}_\beta^W(z)} dz \right] \\
 &= \frac{\partial Z_\beta^{-1}}{\partial \beta} \int [\tilde{\pi}_1(z) - \tilde{\pi}_0(z)] dz \\
 &= -\frac{1}{Z_\beta^2} \frac{\partial Z_\beta}{\partial \beta} \int [\tilde{\pi}_1(z) - \tilde{\pi}_0(z)] dz \\
 &= -\frac{1}{Z_\beta^2} \left( \int [\tilde{\pi}_1(z) - \tilde{\pi}_0(z)] dz \right)^2 \leq 0
 \end{aligned} \tag{30}$$

This proves Wasserstein thermodynamic local evidence curve is non-increasing. Since

$$\begin{aligned}
 \tilde{\pi}_0(z) &= q_\phi(z|x), \quad Z_0 = \int q_\pi(z|x) dz = 1, \\
 \tilde{\pi}_1(z) &= p_\theta(x, z), \quad Z_1 = \int p_\theta(x, z) dz = p_\theta(x).
 \end{aligned} \tag{31}$$

Since  $h(\beta)$  is non-increasing,

$$\begin{aligned}
 h(0) &= \mathbb{E}_{\pi_0} \left[ \frac{\tilde{\pi}_1 - \tilde{\pi}_0}{\tilde{\pi}_0^W} \right] \\
 &= \int [\tilde{\pi}_1(z) - \tilde{\pi}_0(z)] dz \\
 &\leq \int \tilde{\pi}_1(z) \log \frac{\tilde{\pi}_1(z)}{\tilde{\pi}_0(z)} dz = Z_1 \cdot \text{EUBO}.
 \end{aligned} \tag{32}$$

where the last inequality follows from Lemma (S2) below.

$$\begin{aligned}
 h(1) &= \mathbb{E}_{\pi_1} \left[ \frac{\tilde{\pi}_1 - \tilde{\pi}_0}{\tilde{\pi}_1} \right] \\
 &= \int \frac{\pi_1}{\tilde{\pi}_1} [\tilde{\pi}_1 - \tilde{\pi}_0] dz \\
 &= \frac{\int [\tilde{\pi}_1 - \tilde{\pi}_0] dz}{Z_1} \geq \frac{1}{Z_1} \text{ELBO}
 \end{aligned} \tag{33}$$

where we have applied Lemma (S2) again for the inequality.  $\square$

**Lemma S2.** When  $f, g > 0$ , the following inequalities hold.

$$f - g \leq f \log \frac{f}{g}, \quad f - g \geq g \log \frac{f}{g}. \tag{34}$$

*Proof.* Denote  $x = \frac{f}{g} > 0$ .

$$\begin{aligned}
 \frac{f-g}{f} &= 1 - \frac{1}{x} \leq \log x = \log \frac{f}{g} \\
 \frac{f-g}{g} &= x - 1 \geq \log x = \log \frac{f}{g}.
 \end{aligned} \tag{35}$$

$\square$

### C.3 Proof of Proposition 3.3 (Monotonicity of HBO)

*Proof.* Recall  $\log p_\theta(x) = \int_0^1 g_\alpha(\beta) d\beta$ , where  $g_\alpha(\beta) = \mathbb{E}_{\pi_{\alpha,\beta}} [U'_{\alpha,\beta}(z)]$ . For  $\alpha \neq 0$ ,

$$U_{\alpha,\beta} = \log \tilde{\pi}_{\alpha,\beta}, \quad U'_{\alpha,\beta} = \frac{\partial U_{\alpha,\beta}}{\partial \beta} = \frac{1}{\tilde{\pi}_{\alpha,\beta}} \frac{\partial \tilde{\pi}_{\alpha,\beta}}{\partial \beta} = \frac{1}{\alpha} \frac{\tilde{\pi}_1^\alpha - \tilde{\pi}_0^\alpha}{\tilde{\pi}_{\alpha,\beta}^\alpha}, \quad (36)$$

$$U''_{\alpha,\beta} = \frac{\partial^2 U_{\alpha,\beta}}{\partial \beta^2} = -\frac{1}{\alpha} \frac{(\tilde{\pi}_1^\alpha - \tilde{\pi}_0^\alpha)^2}{\tilde{\pi}_{\alpha,\beta}^{2\alpha}} = -\alpha \left( U'_{\alpha,\beta} \right)^2. \quad (37)$$

Via direct computation, we have

$$\frac{\partial}{\partial \beta} g_\alpha(\beta) = \frac{\partial}{\partial \beta} \mathbb{E}_{\pi_{\alpha,\beta}} [U'_{\alpha,\beta}(z)] = \int \frac{\partial}{\partial \beta} [\pi_{\alpha,\beta}(z) U'_{\alpha,\beta}(z)] dz \quad (38)$$

$$= \int \frac{\partial}{\partial \beta} \left[ \frac{\tilde{\pi}_{\alpha,\beta}(z)}{Z_{\alpha,\beta}} U'_{\alpha,\beta}(z) \right] dz \quad (39)$$

$$= \int \frac{1}{Z_{\alpha,\beta}} \frac{\partial \tilde{\pi}_{\alpha,\beta}(z)}{\partial \beta} U'_{\alpha,\beta}(z) dz - \int \frac{\tilde{\pi}_{\alpha,\beta}(z)}{Z_{\alpha,\beta}^2} \frac{\partial Z_{\alpha,\beta}}{\partial \beta} U'_{\alpha,\beta}(z) dz \quad (40)$$

$$+ \int \frac{\tilde{\pi}_{\alpha,\beta}(z)}{Z_{\alpha,\beta}} U''_{\alpha,\beta}(z) dz \quad (41)$$

$$= \int \frac{\tilde{\pi}_{\alpha,\beta}(z)}{Z_{\alpha,\beta}} \frac{\partial \log \tilde{\pi}_{\alpha,\beta}(z)}{\partial \beta} U'_{\alpha,\beta}(z) dz + \int \frac{\tilde{\pi}_{\alpha,\beta}(z)}{Z_{\alpha,\beta}} U''_{\alpha,\beta}(z) dz \quad (42)$$

$$- \int \frac{\tilde{\pi}_{\alpha,\beta}(z)}{Z_{\alpha,\beta}} U'_{\alpha,\beta}(z) dz \int \frac{1}{Z_{\alpha,\beta}} \frac{\partial \tilde{\pi}_{\alpha,\beta}(z)}{\partial \beta} dz \quad (43)$$

$$= \int \pi_{\alpha,\beta}(z) (U'_{\alpha,\beta})^2 dz - \int \pi_{\alpha,\beta}(z) U'_{\alpha,\beta}(z) dz \int \frac{\tilde{\pi}_{\alpha,\beta}(z)}{Z_{\alpha,\beta}} U'_{\alpha,\beta}(z) dz \quad (44)$$

$$+ \int \frac{\tilde{\pi}_{\alpha,\beta}(z)}{Z_{\alpha,\beta}} U''_{\alpha,\beta}(z) dz \quad (45)$$

$$= \mathbb{E}_{\pi_{\alpha,\beta}(z)} [(U'_{\alpha,\beta}(z))^2] - (\mathbb{E}_{\pi_{\alpha,\beta}(z)} [U'_{\alpha,\beta}(z)])^2 + \mathbb{E}_{\pi_{\alpha,\beta}(z)} [U''_{\alpha,\beta}(z)] \quad (46)$$

$$= \mathbb{E}_{\pi_{\alpha,\beta}(z)} [(U'_{\alpha,\beta}(z))^2] - (\mathbb{E}_{\pi_{\alpha,\beta}(z)} [U'_{\alpha,\beta}(z)])^2 - \alpha \mathbb{E}_{\pi_{\alpha,\beta}(z)} [(U'_{\alpha,\beta}(z))^2] \quad (47)$$

$$= \text{Var}_{\pi_{\alpha,\beta}(z)} [U'_{\alpha,\beta}(z)] - \alpha \mathbb{E}_{\pi_{\alpha,\beta}(z)} [(U'_{\alpha,\beta}(z))^2] \quad (48)$$

$$= -(\mathbb{E}_{\pi_{\alpha,\beta}(z)} [U'_{\alpha,\beta}(z)])^2 + (1 - \alpha) \mathbb{E}_{\pi_{\alpha,\beta}(z)} [(U'_{\alpha,\beta}(z))^2] \quad (49)$$

Therefore, when  $\alpha \leq 0$  then  $\partial_\beta g_\alpha(\beta) \geq 0$ , so  $g_\alpha(\beta)$  is non-decreasing; and when  $\alpha \geq 1$  then  $\partial_\beta g_\alpha(\beta) \leq 0$ , and  $g_\alpha(\beta)$  is non-increasing.  $\square$

### C.4 Derivation for the Importance Weighted HBO

*Proof.* For simplicity, let us denote

$$s = \left( \frac{p(\mathbf{x}, \mathbf{z})}{q(\mathbf{z})} \right)^\alpha, \quad \text{and } t = s - 1 \quad (50)$$

The the (unnormalized) importance weight  $\tilde{\pi}/q$  can be expressed as

$$\frac{\tilde{\pi}_{\alpha,\beta}(\mathbf{z})}{q(\mathbf{z})} = \left[ \beta \left( \frac{p}{q} \right)^\alpha + (1 - \beta) \right]^{1/\alpha} = (\beta \cdot t + 1)^{1/\alpha} \quad (51)$$

Given a set of empirical samples  $\{\mathbf{z}_i\}_{i=1}^m$  from  $q_\phi(\mathbf{z}|\mathbf{x})$ , the self-normalized importance weights are given by

$$\bar{w}_{\alpha,i}^\beta = w_{\alpha,i}^\beta / \sum_i w_{\alpha,i}^\beta, \quad (52)$$

where  $w_{\alpha,i}^\beta = (\beta \cdot t_i + 1)^{1/\alpha}$ . And on the other hand, we have the integrand for the local evidence term given by

$$U'_{\alpha,\beta} = \frac{p^\alpha - q^\alpha}{\alpha \pi_{\alpha,\beta}^\alpha} = \frac{t}{\alpha(\beta t + 1)} \quad (53)$$

Plugging into the empirical self-normalized importance weighted estimator,

$$\mathbb{E}_{\pi_{\alpha,\beta}}[f(\mathbb{Z})] \approx \sum_i \left[ \bar{w}_{\alpha,i}^\beta \cdot f(\mathbf{z}_i) \right] \quad (54)$$

this gives us

$$\mathcal{E}_{\alpha,\beta} = \mathbb{E}_{\pi_{\alpha,\beta}}[U'_{\alpha,\beta}] \quad (55)$$

$$\approx \sum_i \frac{t_i}{\alpha(\beta t_i + 1)} \bar{w}_{\alpha,i}^\beta \quad (56)$$

$$= \sum_i \frac{t_i}{\alpha(\beta t_i + 1)} \frac{(\beta \cdot t_i + 1)^{1/\alpha}}{\sum_{i'} (\beta t_{i'} + 1)^{1/\alpha}} \quad (57)$$

$$= \frac{1}{\alpha \sum_{i'} (\beta t_{i'} + 1)^{1/\alpha}} \sum_i \frac{t_i}{(\beta t_i + 1)^{1-1/\alpha}} \quad (58)$$

□

## C.5 Derivation for the Perturbed HBO Estimator

*Proof.* To construct a perturbed estimator for HBO =  $\int \mathbb{E}_{\pi_{\alpha,\beta}}[U'_{\alpha,\beta}] d\beta$  wrt parameter  $\alpha$ , we will need Taylor expansions for both the integrand  $U'_{\alpha,\beta}$  and path density  $\pi_{\alpha,\beta}$ . The following facts are handy for our derivations

$$\tilde{\pi}_{\alpha,\beta}^\alpha = \beta \tilde{\pi}_1^\alpha + (1 - \beta) \tilde{\pi}_0^\alpha \quad (59)$$

$$\lim_{\alpha \rightarrow 0} \tilde{\pi}_{\alpha,\beta}^\alpha = 1 \quad (60)$$

$$\partial_\alpha \tilde{\pi}_{\alpha,\beta}^\alpha = \beta \tilde{\pi}_1^\alpha \log \tilde{\pi}_1 + (1 - \beta) \tilde{\pi}_0^\alpha \log \tilde{\pi}_0 \quad (61)$$

$$\lim_{\alpha \rightarrow 0} \partial_\alpha \tilde{\pi}_{\alpha,\beta}^\alpha = \log \left[ \tilde{\pi}_1^\beta \tilde{\pi}_0^{1-\beta} \right]. \quad (62)$$



We first compute the Taylor expansion of integrand  $U'_{\alpha,\beta}$  at  $\alpha = 0$

$$U'_{\alpha,\beta}|_{\alpha=0} = \lim_{\alpha \rightarrow 0} \frac{\tilde{\pi}_1^\alpha - \tilde{\pi}_0^\alpha}{\alpha \tilde{\pi}_{\alpha,\beta}^\alpha} = \lim_{\alpha \rightarrow 0} \frac{\partial_\alpha [\tilde{\pi}_1^\alpha - \tilde{\pi}_0^\alpha]}{\partial_\alpha [\alpha \beta \tilde{\pi}_1^\alpha + \alpha(1-\beta)\tilde{\pi}_0^\alpha]} \quad (63)$$

$$= \lim_{\alpha \rightarrow 0} \frac{\tilde{\pi}_1^\alpha \log \tilde{\pi}_1 - \tilde{\pi}_0^\alpha \log \tilde{\pi}_0}{\beta \tilde{\pi}_1^\alpha (1 + \alpha \log \tilde{\pi}_1) + (1-\beta)\tilde{\pi}_0^\alpha (1 + \alpha \log \tilde{\pi}_0)} \quad (64)$$

$$= \log \tilde{\pi}_1 - \log \tilde{\pi}_0 \rightarrow U'_{0,\beta} \quad (65)$$

$$\partial_\alpha U'_{\alpha,\beta}|_{\alpha=0} = \lim_{\alpha \rightarrow 0} \frac{\partial}{\partial \alpha} \left[ \frac{\tilde{\pi}_1^\alpha - \tilde{\pi}_0^\alpha}{\alpha \tilde{\pi}_{\alpha,\beta}^\alpha} \right] \quad (66)$$

$$= \lim_{\alpha \rightarrow 0} \left( \underbrace{-\frac{1}{\alpha^2} \frac{\tilde{\pi}_1^\alpha - \tilde{\pi}_0^\alpha}{\tilde{\pi}_{\alpha,\beta}^\alpha}}_{T_1} + \underbrace{\frac{1}{\alpha} \frac{\tilde{\pi}_1^\alpha \log \tilde{\pi}_1 - \tilde{\pi}_0^\alpha \log \tilde{\pi}_0}{\tilde{\pi}_{\alpha,\beta}^\alpha}}_{T_2} - \underbrace{\frac{\tilde{\pi}_1^\alpha - \tilde{\pi}_0^\alpha}{\alpha \tilde{\pi}_{\alpha,\beta}^{2\alpha}} \partial_\alpha \tilde{\pi}_{\alpha,\beta}^\alpha}_{T_3} \right) \quad (67)$$

$$\lim_{\alpha \rightarrow 0} T_1 = - \lim_{\alpha \rightarrow 0} \frac{\tilde{\pi}_1^\alpha \log \tilde{\pi}_1 - \tilde{\pi}_0^\alpha \log \tilde{\pi}_0}{2\alpha \tilde{\pi}_{\alpha,\beta}^\alpha + \alpha^2 \partial_\alpha \tilde{\pi}_{\alpha,\beta}^\alpha} \quad (68)$$

$$= - \lim_{\alpha \rightarrow 0} \frac{\tilde{\pi}_1^\alpha (\log \tilde{\pi}_1)^2 - \tilde{\pi}_0^\alpha (\log \tilde{\pi}_0)^2}{2\tilde{\pi}_{\alpha,\beta}^\alpha + 4\alpha \partial_\alpha \tilde{\pi}_{\alpha,\beta}^\alpha + \alpha^2 \partial_\alpha^2 \tilde{\pi}_{\alpha,\beta}^\alpha} = - \frac{(\log \tilde{\pi}_1)^2 - (\log \tilde{\pi}_0)^2}{2} \quad (69)$$

$$\lim_{\alpha \rightarrow 0} T_2 = \lim_{\alpha \rightarrow 0} \frac{\tilde{\pi}_1^\alpha (\log \tilde{\pi}_1)^2 - \tilde{\pi}_0^\alpha (\log \tilde{\pi}_0)^2}{\tilde{\pi}_{\alpha,\beta}^\alpha + \alpha \partial_\alpha \tilde{\pi}_{\alpha,\beta}^\alpha} = (\log \tilde{\pi}_1)^2 - (\log \tilde{\pi}_0)^2 \quad (70)$$

$$\lim_{\alpha \rightarrow 0} T_3 = \lim_{\alpha \rightarrow 0} \frac{(\tilde{\pi}_1^\alpha \log \tilde{\pi}_1 - \tilde{\pi}_0^\alpha \log \tilde{\pi}_0) \partial_\alpha \tilde{\pi}_{\alpha,\beta}^\alpha - (\tilde{\pi}_1^\alpha - \tilde{\pi}_0^\alpha) \partial_\alpha^2 \tilde{\pi}_{\alpha,\beta}^\alpha}{\tilde{\pi}_{\alpha,\beta}^{2\alpha} + 2\tilde{\pi}_{\alpha,\beta}^\alpha \partial_\alpha \tilde{\pi}_{\alpha,\beta}^\alpha} \quad (71)$$

$$= \log [\tilde{\pi}_1 \tilde{\pi}_0^{-1}] \log \left[ \tilde{\pi}_1^\beta \tilde{\pi}_0^{1-\beta} \right] \quad (72)$$

Putting everything together, we have

$$\partial_\alpha U'_{\alpha,\beta}|_{\alpha=0} = (\log \tilde{\pi}_1 - \log \tilde{\pi}_0)^2 \left( \frac{1}{2} - \beta \right) \rightarrow \partial_\alpha U'_{0,\beta} \quad (73)$$

$$U'_{\delta,\beta} \approx (\log \tilde{\pi}_1 - \log \tilde{\pi}_0) + (\log \tilde{\pi}_1 - \log \tilde{\pi}_0)^2 \left( \frac{1}{2} - \beta \right) \delta + \mathcal{O}(\delta)^2 \quad (74)$$

For the path density, we consider its unnormalized form

$$\partial_\alpha \log \tilde{\pi}_{\alpha,\beta} = - \underbrace{\frac{1}{\alpha^2} \log (\beta \tilde{\pi}_1^\alpha + (1-\beta)\tilde{\pi}_0^\alpha)}_{I_1} + \underbrace{\frac{\beta \tilde{\pi}_1^\alpha \log \tilde{\pi}_1 + (1-\beta)\tilde{\pi}_0^\alpha \log \tilde{\pi}_0}{\alpha (\beta \tilde{\pi}_1^\alpha + (1-\beta)\tilde{\pi}_0^\alpha)}}_{I_2} \quad (75)$$

$$\lim_{\alpha \rightarrow 0} I_1 = \lim_{\alpha \rightarrow 0} \frac{\beta \tilde{\pi}_1^\alpha \log \tilde{\pi}_1 + (1-\beta)\tilde{\pi}_0^\alpha \log \tilde{\pi}_1}{2\alpha (\beta \tilde{\pi}_1^\alpha + (1-\beta)\tilde{\pi}_0^\alpha)} \quad (76)$$

$$= \lim_{\alpha \rightarrow 0} \frac{\beta \tilde{\pi}_1^\alpha (\log \tilde{\pi}_1)^2 + (1-\beta)\tilde{\pi}_0^\alpha (\log \tilde{\pi}_0)^2}{2(\beta \tilde{\pi}_1^\alpha + (1-\beta)\tilde{\pi}_0^\alpha)} \quad (77)$$

$$= \frac{1}{2} [\beta (\log \tilde{\pi}_1)^2 + (1-\beta) (\log \tilde{\pi}_0)^2] \quad (78)$$

$$\lim_{\alpha \rightarrow 0} I_2 = \lim_{\alpha \rightarrow 0} \frac{\beta \tilde{\pi}_1^\alpha (\log \tilde{\pi}_1)^2 + (1-\beta)\tilde{\pi}_0^\alpha (\log \tilde{\pi}_0)^2}{\beta \tilde{\pi}_1^\alpha + (1-\beta)\tilde{\pi}_0^\alpha} \quad (79)$$

$$= \beta (\log \tilde{\pi}_1)^2 + (1-\beta) (\log \tilde{\pi}_0)^2 \quad (80)$$

$$\lim_{\alpha \rightarrow 0} \partial_\alpha \log \tilde{\pi}_{\alpha,\beta} = \frac{1}{2} [\beta (\log \tilde{\pi}_1)^2 + (1-\beta) (\log \tilde{\pi}_0)^2] \quad (81)$$

$$\log \tilde{\pi}_{\delta,\beta} \approx (\beta \log \tilde{\pi}_1 + (1-\beta) \log \tilde{\pi}_0) + \frac{1}{2} [\beta (\log \tilde{\pi}_1)^2 + (1-\beta) (\log \tilde{\pi}_0)^2] \delta \quad (82)$$

This concludes our proof.  $\square$

## D Experimental Setups

### D.1 Datasets

The following datasets are considered in the current study.

- **MNIST** a handwritten digit database with 70k binarized  $28 \times 28$  images. Following standard split, we use 60k for development (5/1 split for training and validation) and the rest 10k for test.
- **Omniglot** Lake et al. (2015) is a dataset of 1623 handwritten characters across 50 alphabets. Each data point is a binarized  $28 \times 28$  image. We split the dataset into 24,345 for training and 8,070 for testing.
- **Cifar10** Krizhevsky et al. (2009) consists of 60k size  $32 \times 32$  colour images from 10 classes. We split the dataset into 50k training and 10k for testing.
- **CelebA** Liu et al. (2018) consists more than 200k celebrity images. We split the dataset into 162,770 training and 19,962 for testing.
- **Yelp** Shen et al. (2017); Yang et al. (2017) contains more than 100,000 long sentences with average length equals 96.7. We split the dataset into 100,000 training sentences, 10,000 for validation and 10,000 for test.

### D.2 Numerical integration

To compute an approximation to the log-likelihood, we need to numerically integrate the local evidence along the thermodynamic curve. We consider the following partition schemes for varying budget  $K \in [2, 5, 10, 30, 50]$ :

- Log partition: fix  $\beta_0 = 0$ , split the interval  $[\beta_1, 1]$  evenly on a log scale. We follow the original TVO paper Masrani et al. (2019) choose  $\beta_1 = 10^{-1.09}$  for a large number of partition.
- Uniform partition: split the interval  $[0, 1]$  evenly on a linear scale.

We have compared the following three integration strategies,

- Trapez:  $\sum_{i=0}^{K-1} (\beta_{i+1} - \beta_i) \cdot \frac{f(\beta_i) + f(\beta_{i+1})}{2}$ ,
- Left:  $\sum_{i=0}^{K-1} (\beta_{i+1} - \beta_i) \cdot f(\beta_i)$ ,
- Right:  $\sum_{i=0}^{K-1} (\beta_{i+1} - \beta_i) \cdot f(\beta_{i+1})$ .

### D.3 Model architectures (standard)

Following Kingma and Welling (2014); Burda et al. (2016), we use the standard Gaussian for the prior and conditional Gaussian for the approximate posterior, unless otherwise specified, with the mean and diagonal covariance parameterized by deep neural net. The conditional likelihood model is set to Bernoulli for binary responses and Gaussian for continuous responses (for simplicity we fix the variance to 1).

$$\begin{aligned}
 p_\theta(\mathbf{x}, \mathbf{z}) &= p_\theta(\mathbf{x}|\mathbf{z})p(\mathbf{z}), \\
 p(\mathbf{z}) &= \text{Normal}(\mathbf{z}|0, I), \\
 p_\theta(\mathbf{x}|\mathbf{z}) &= \text{Bernoulli}(\mathbf{x}|\text{decoder}_\theta(\mathbf{z})) \text{ or } p_\theta(\mathbf{x}|\mathbf{z}) = \text{Normal}(\mathbf{x}|\text{decoder}_\theta(\mathbf{z}), \sigma^2) \\
 q_\phi(\mathbf{z}|\mathbf{x}) &= \text{Normal}(\mathbf{z}|\mu_\phi(\mathbf{x}), \sigma_\phi(\mathbf{x}))
 \end{aligned} \tag{83}$$

For MNIST and Omniglot dataset, we use two-layer MLPs with tanh activation as encoder. The output of the encoder is duplicated and passed through an additional linear layer to parameterize the mean and log-standard deviation of a 200 hidden dimensions conditionally independent Normal distribution. The decoder is a three-layer MLP with tanh activations and sigmoid output which parameterizes the probabilities of the Bernoulli distribution.

For Cifar10 dataset, we use three-layer Conv2d (filters:  $64 \times 4 \times 4 - 128 \times 4 \times 4 - 512 \times 4 \times 4$ ) with ReLU activation as encoder (Chen et al., 2021b). The latent representation first passes through a Dense layer, then a three-layer DeConv2d decoder (filters:  $256 \times 4 \times 4 - 64 \times 4 \times 4 - 3 \times 4 \times 4$ ) with ReLU activations. We set hidden dimensions to 1024.

For CelebA dataset, we use the five-layer Conv2d ( $32 \times 4 \times 4 - 64 \times 4 \times 4 - 128 \times 4 \times 4 - 256 \times 4 \times 4 - 512 \times 4 \times 4$ ). The decoder is a five-layer Upsampling Conv2d network where the filter size and kernel size are the reverse of the encoder. Each Conv2d layer in the decoder follows a upsampling layer. For both encoder and decoder, we choose LeakyReLU as activation and add a BN layer after each Conv2d layer.

For Yelp dataset, we implement both encoder and decoder as one-layer LSTMs with 1024 hidden units and 512-dimensional word embeddings. The vocabulary size is 20K. The last hidden state of the encoder concatenated with a 32-dimensional Gaussian noise is used to sample 32-dimensional latent codes, which is then adopted to predict the initial hidden state of the decoder LSTM and additionally fed as input to each step at the LSTM decoder. A KL-cost annealing strategy is commonly used (Tao et al., 2019b), where the scalar weight on the KL term is increased linearly from 0.1 to 1.0 each batch over 10 epochs. There are dropout layers with probability 0.5 between the input-to-hidden layer and the hidden-to-output layer on the decoder LSTM only.

All the parameters for the image model are initialized at random and optimized using ADAM.

#### D.4 Inference with normalizing flows

To enable more flexible posterior approximation, we consider empowering  $q_\phi(z|x)$  with normalizing flows (Rezende and Mohamed, 2015). We modified the Karpathy’s `Torch` implementation of flows <sup>6</sup> (*e.g.*, adding conditional flow support), and replace standard encoder with a flow-based encoder. To get maximal sampling efficiency, we choose the MAF-based IAF flow as our default choice (Kingma et al., 2016; Papamakarios et al., 2017; Chen et al., 2020). We notice such shift-scale flows sometimes suffer stability issues, which can be remedied by the slower alternatives (Papamakarios et al., 2019), such as spline flows (Durkan et al., 2019).

#### D.5 Baselines and specifications

We consider the following representative or popular baselines to benchmark our HBO.

- ELBO/VAE: Kingma and Welling (2014) Vanilla ELBO
- IW-ELBO/IW-VAE: Burda et al. (2016) Importance weighted ELBO. We set importance samples to 10.
- Rényi: Li and Turner (2016) We use the Rényi-Max variant which reported best performance in the original Rényi paper
- TVO: Masrani et al. (2019) Thermodynamics variational objective

For fair comparison, other aspects are all matched.

## E Additional Results and Analyses for Synthetic Examples

### E.1 Bayesian regression

To benchmark HBO’s performance against other bounds, we consider Bayesian parameter estimation for regression problems. Specifically, we consider the classic toy model given below, given assigns a non-informative prior:

$$Y = \alpha + \beta \tilde{X} + \epsilon, \quad X = \tilde{X} + \zeta \quad (84)$$

$$p(\alpha, \beta) \propto (1 + \beta^2)^{-3/2}, \quad p(\sigma) \propto \frac{1}{\sigma}. \quad (85)$$

where  $\epsilon, \zeta \sim \mathcal{N}(0, \sigma^2)$ ,  $\tilde{X} = \mathcal{U}[0, 100]$ , and observations are given in pairs of  $\mathcal{D} = \{(x_i, y_i)\}_{i=1}^n$ . We set ground-truth parameters to  $\alpha = 25, \beta = 0.5, \sigma^2 = 10$ , and sample  $n = 20$  points. The goal is to inference the posterior

<sup>6</sup><https://github.com/karpathy/pytorch-normalizing-flows/>

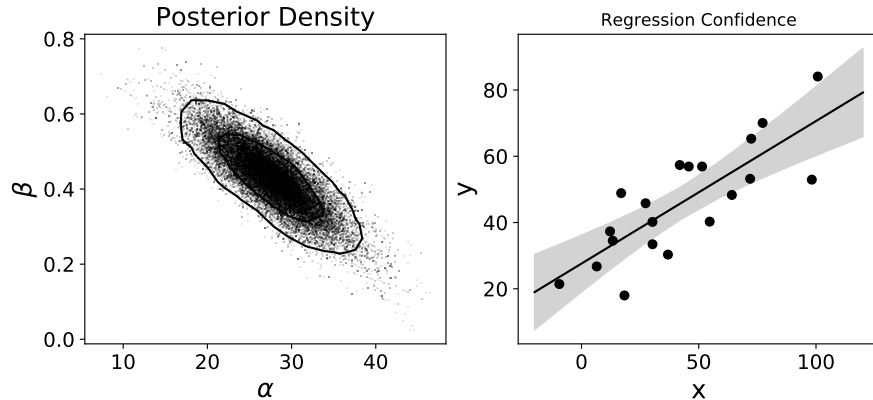


Figure S8: MCMC posterior (left) and model fit (right) for Eqn (84-85). Dots are data points, solid line fitted curve, and shaded region confidence intervals.

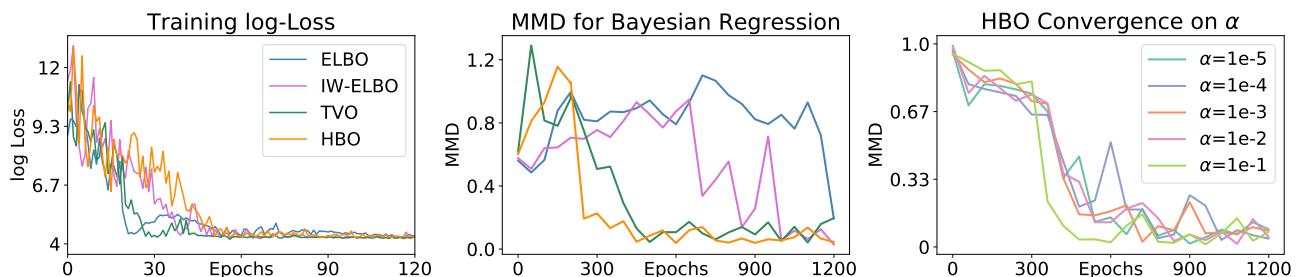


Figure S9: Convergence plot for different objectives. (left) training loss; (middle) MMD loss for different bounds; (right) MMD loss for different HBO( $\alpha$ ). Lower is better.

distribution  $p(\alpha, \beta, \sigma | \mathcal{D})$ . We use the `emcee`<sup>7</sup> package to draw MCMC samples as ground-truth reference (See Figure S8).

In Figure 5.1 we examine the convergence of different VI criteria quantitatively. Specifically, we appeal to the *maximal mean discrepancy* (MMD) metric (Gretton et al., 2012) to evaluate the similarity between the ground-truth posterior to the variational approximations. Since the original scale of parameters differ, we use the mean and standard deviation of the true posterior to normalize all sample estimates, and set kernel bandwidth parameter to 0.5. We use 5k MCMC samples as the reference distribution and find the results sufficiently stable. As we can see, HBO delivers the fastest convergence to ground-truth, followed by TVO and then IW-ELBO. Vanilla ELBO struggles the most. This is consistent with the theoretical predictions of the tightness of the bounds. We further carried out the ablation study to examine the convergence for different HBO( $\alpha$ ).

## E.2 Bayesian inference for complex posterior

To make the inference more challenging, we consider the following model:

$$y = \sqrt{z_1^2 + z_2^2} + \xi, z_1, z_2 \sim \mathcal{N}(0, 1), \xi \sim \mathcal{N}(0, 0.1^2), \quad (86)$$

and the goal is to infer pair  $(z_1, z_2)$  given an observation  $y$ . The posterior will be circle-like for a sufficiently large  $y$  (see Figure S1), and here we focus on the case where  $y = 1$ .

<sup>7</sup><https://emcee.readthedocs.io/en/stable/>

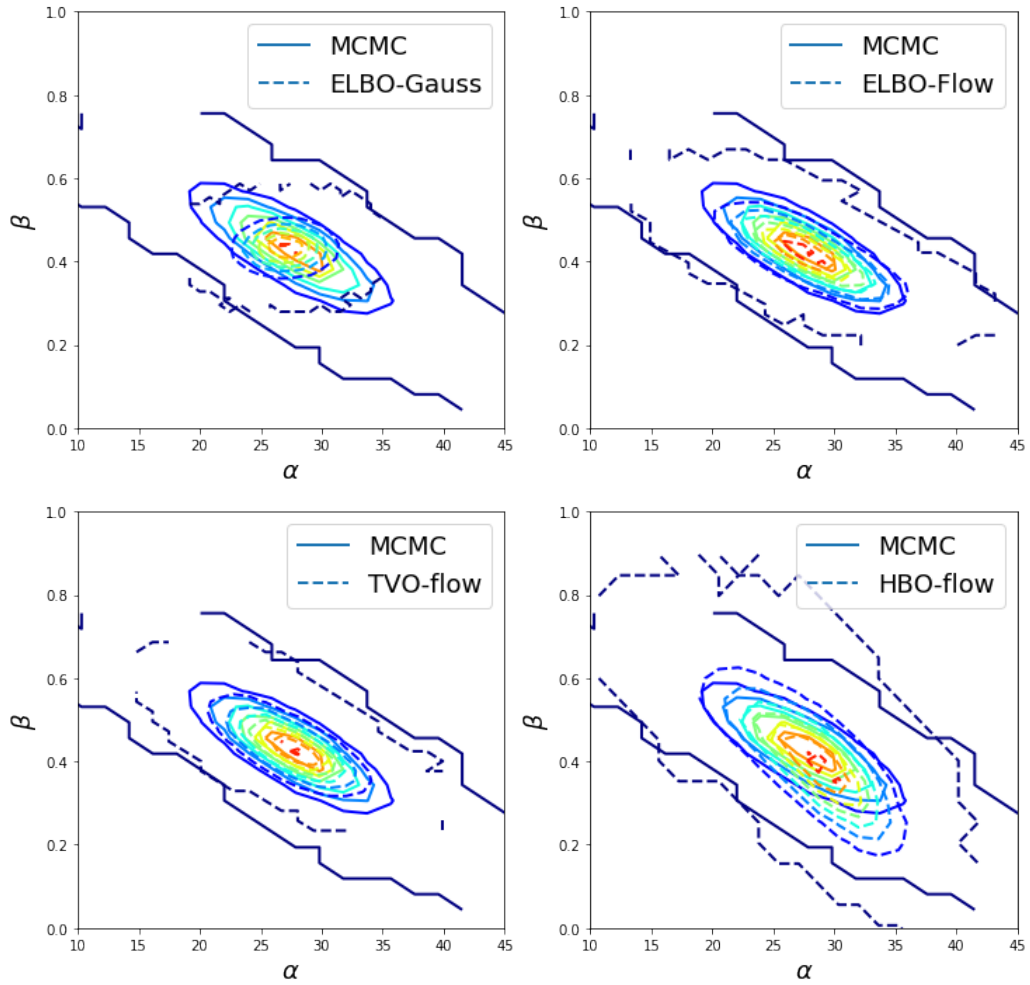


Figure S10: Comparison of posterior estimates from different variational objectives, overlaid on ground-truth contours.

## F Additional Results and Analyses for Real-World Datasets

In Figure S11 we compare the effective sample-size (ESS) (Chen et al., 2021a) of different schemes on MNIST. To come up with a single summarizing statistics, ESS is averaged along the discretized thermodynamics path. Consistent with our analysis from the toy model, HBO shows better latent sample efficiency compared with other alternatives with a sharper bound.

In Figure S12 we visualize the spread of ELBO evaluation comparing the utility of learned posterior respectively learned from TVO and HBO. It shows posterior samples from HBO are more likely relative to those from TVO. We also examined Rényi, but it shows and more generated profile, and therefore we removed it from our presentation for visual clarity.

Figure S13 plots a few thermodynamic local evidence curve corresponding to different  $\alpha$ . We see the phase transition (*i.e.*, flipped monotonicity) happening. Note that the best curve does not seem strictly flat, which can be potentially attributed to the approximation error originated from our perturbed estimator and the importance weighting scheme.

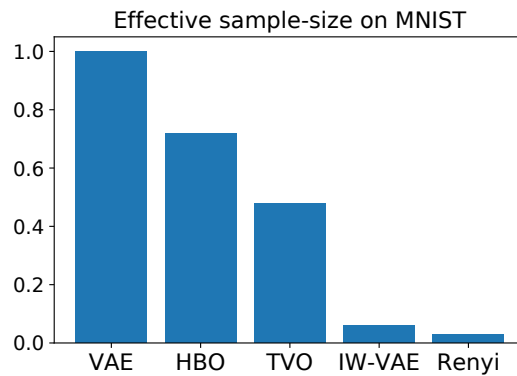


Figure S11: Comparison of effective sample-size with different VI objectives on MNIST.

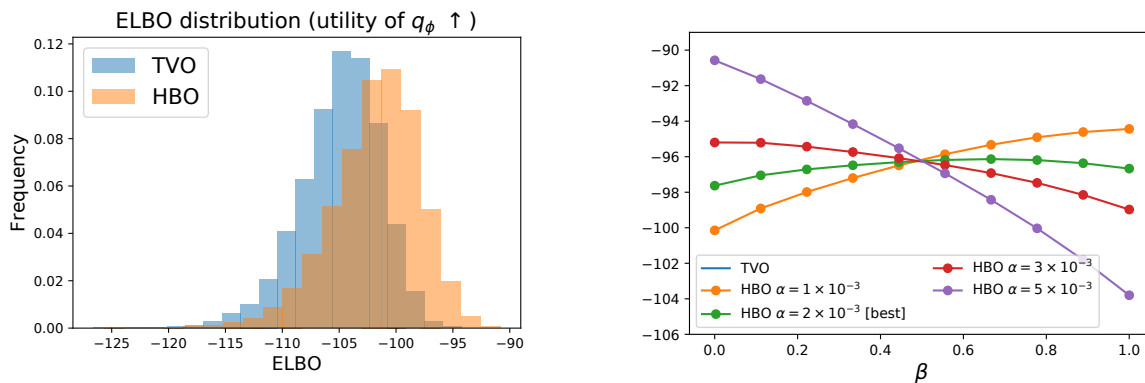


Figure S12: Distribution of local evidence (ELBO) using models respectively trained with TVO and HBO.

Figure S13: HBO curves for different  $\alpha$  on MNIST.





Figure S14: Samples generated from the HBO model on MNIST.

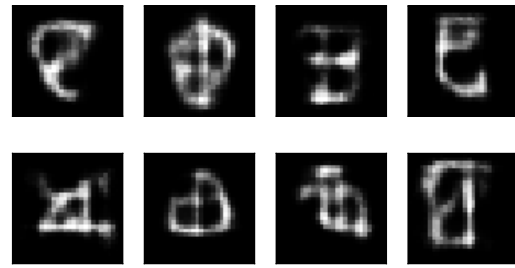


Figure S15: Samples generated from the HBO model on Omniglot.



Figure S16: Samples reconstructed from Cifar.

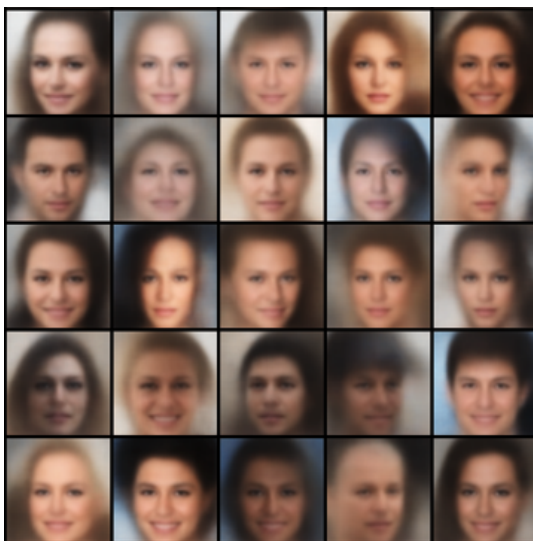


Figure S17: Samples generated from CelebA.

Original: "i/sj slow service , rude hostess and cold food . what 's the point when you have so many options ? i/sj"

VAE: "food service . food rude , rude beer . the a not point of you 're to many bad for i/sj"

HBO: "the service . slow staff , the food . i/sj a the point of you are a much people for i/sj"

Samples reconstructed from Yelp.